Quantitative Microstructural Analysis of Cellular and Tissue Remodeling in Human Glaucoma Optic Nerve Head

Carolyn Guan,[1] Mary Ellen Pease,[1] Sarah Quillen,[1] Yik Tung Tracy Ling,[2] Ximin Li,[3] Elizabeth Kimball,[1] Thomas V. Johnson,[1] Thao D. Nguyen,[1,2] and Harry A. Quigley[1]

[1]Wilmer Ophthalmological Institute, School of Medicine, The Johns Hopkins University, Baltimore, Maryland, United States
[2]Departments of Mechanical Engineering and Materials Science & Engineering, The Johns Hopkins University, Baltimore, Maryland, United States
[3]Department of Biostatistics, The Bloomberg School of Public Health, The Johns Hopkins University, Baltimore, Maryland, United States

Correspondence: Mary Ellen Pease, Glaucoma Center of Excellence, Wilmer Eye Institute, The Johns Hopkins University School of Medicine, 400 North Broadway, M029 Smith Building, Baltimore, MD 21231, USA;
mpease@jhmi.edu.

CG and MEP contributed equally to the work presented here and should therefore be regarded as equivalent authors.

PURPOSE. To measure quantitatively changes in lamina cribrosa (LC) cell and connective tissue structure in human glaucoma eyes.

METHODS. We studied 27 glaucoma and 19 age-matched non-glaucoma postmortem eyes. In 25 eyes, LC cross-sections were examined by confocal and multiphoton microscopy to quantify structures identified by anti-glial fibrillary acidic protein (GFAP), phalloidin-labeled F-actin, nuclear 4′,6-diamidino-2-phenylindole (DAPI), and by second harmonic generation imaging of LC beams. Additional light and transmission electron microscopy were performed in 21 eyes to confirm features of LC remodeling, including immunolabeling by anti-SOX9 and anti-collagen IV. All glaucoma eyes had detailed clinical histories of open-angle glaucoma status, and degree of axon loss was quantified in retrolaminar optic nerve cross-sections.

RESULTS. Within LC pores, the proportionate area of both GFAP and F-actin processes was significantly lower in glaucoma eyes than in controls ($P = 0.01$). Nuclei were rounder (lower median aspect ratio) in glaucoma specimens ($P = 0.02$). In models assessing degree of glaucoma damage, F-actin process width was significantly wider in glaucoma eyes with more damage ($P = 0.024$), average LC beam width decreased with worse glaucoma damage ($P = 0.042$), and nuclear count per square millimeter rose with worse damage ($P = 0.019$). The greater cell count in LC pores represented 92.3% astrocytes by SOX9 labeling. The results are consistent with replacement of axons in LC pores by basement membrane labeled by anti-collagen IV and in-migrating astrocytes.

CONCLUSIONS. Alteration in LC structure in glaucoma involves migration of astrocytes into axonal bundles, change in astrocyte orientation and processes, production of basement membrane material, and thinning of connective tissue beams.

Keywords: glaucoma, lamina cribrosa, optic nerve head, astrocyte, microglia

An important site of damage to retinal ganglion cell (RGC) axons in glaucoma is the lamina cribrosa (LC) of the optic nerve head (ONH).[1–4] The intraocular pressure (IOP) generates mechanical stress in the sclera and the ONH, producing strains that have detrimental effects on RGC axons, ONH astrocytes, and nutritional blood flow in the ONH.[5–9] The peripapillary sclera (PPS) consists of a circumferential pattern of collagen, elastin, and fibroblasts and a non-fibrous matrix whose overall configuration is designed to resist the circumferential expansion of the ONH from IOP increase (hoop stress). The remainder of the sclera has a basket-weave pattern of alternating and interdigitating fiber bundles.[10–14] The connective tissue beams of LC contain collagen and elastin lined by astrocytes, which course across the ONH opening at the level of the sclera.[15–19] Both the fibrous and matrix elements of the ONH and scleral connective tissues are important to their mechanical behavior.[20,21] The responses of the sclera and ONH to the level of IOP are potential biomarkers and translational opportunities for glaucoma incidence and progression.[22]

In experimental non-human primate glaucoma[23–26] and human glaucoma eyes,[27–29] the structures of the sclera and ONH are remodeled, with loss of the circumferential arrangement of PPS fibers and with deepening and widening of the LC. In primates and mice, the ONH structure is maintained by resident fibroblasts and astrocytes.[30–34] The cells of the ONH (neuronal axons, glia, and fibroblasts) are suggested to be mechanosensitive.[35–39] Regional differences[40–42] in connective tissue density and pore size within the LC lead to greater regional ONH strains[43–45] producing selective death of RGC axons in the upper and lower poles of the ONH.[4] IOP-generated stress is translated through the

interaction between PPS and ONH that has been studied in theoretical models.[46,47] Experimental therapeutic alteration of sclera and ONH properties can lead to either detrimental[48,49] or beneficial effects[50] on RGC axonal survival.

There are various reports of histological features of glaucoma-related remodeling of the ONH and sclera in both human eyes and animal models. Few of these investigations have been able to document quantitatively the cellular and connective tissue alterations in human glaucoma eyes. These changes are likely to be central to the biomechanical behavior that contributes to glaucoma damage. Here, we present measurements of detailed histological differences in the connective tissues, as well as in the axonal and glial components of the ONH, comparing human eyes exhibiting glaucoma damage from mild to severe with age-matched non-glaucoma eyes.

METHODS

Human Subjects Research

This research was approved and supervised by the Institutional Review Board of The Johns Hopkins School of Medicine. The human eyes and the clinical history data were received in deidentified form from eye banks. The use of postmortem human tissues does not qualify as human subjects research under the Common Rule used by the National Institutes of Health. Either the deceased gave permission for eye donation during life or legal representatives gave permission for eye donation. Controls had no history of eye disease.

Demographic Data on Eyes and Persons Included

Whole globes were obtained from the Illinois Eye Bank of Chicago (Chicago, IL), Lions Eye Bank of Oregon (Portland, OR), Lions Gift of Sight (Minneapolis, MN), or through the National Disease Research Interchange (Philadelphia, PA). The requirements for accepting eyes were (1) death to enucleation < 12 hours, (2) death to receipt on ice < 36 hours, and (3) an optic nerve of ≥3 mm in length. Eyes from persons with a history of diabetes or terminal disease including sepsis were excluded. Eyes that were utilized in the serial cross-sectional studies by laser scanning microscopy (LSM) and second harmonic generation (SHG) imaging were selected to age match glaucoma and control groups, as were the glaucoma and control groups in the light and transmission electron microscopy (TEM) studies. See Table 1 for demographic and clinical data for each eye and the corresponding summary data.

In the serial section study set, there were 16 glaucoma eyes from 12 persons. Visual field tests (Zeiss HFA II; Zeiss Meditec, Dublin, CA, USA) were available for 11 eyes of eight persons, with a mean deviation = -7.05 ± 6.8 (range, -0.02 to -17.8) and a mean pattern standard deviation = 5.6 ± 3.4 (range, $1.84–11.64$). Among glaucoma eyes, 15/16 had a history of IOP-lowering drops and known highest IOP mean = 18.2 ± 6.9 mmHg (range, 10–31). Five eyes had had cataract/IOL surgery, and none had had glaucoma surgery. Time of death to enucleation was 4.6 ± 1.7 hours (range, 3–8) in glaucoma eyes and 5.2 ± 2.7 hours (range, 3–9) for controls ($P = 0.5$ for difference from glaucoma eyes).

For the TEM study, there were 11 glaucoma eyes from nine persons; 10 of the 11 eyes had a history of IOP-lowering drops, with known highest IOP mean = 13.7 ± 2.7 mmHg

(range, 8–18). Ten glaucoma eyes had cataract/IOL surgery, and one had laser angle glaucoma surgery. For glaucoma eyes, mean time from death to enucleation was 7.4 ± 4.0 hours (range, 3–14), and it was 4.6 ± 2.1 hours (range, 2–8) for 10 eyes of 10 control persons ($P = 0.07$ for difference from glaucoma eyes).

Labeling of Serial Cross-Sections

Eyes were received in moist chambers on ice within 36 hours of death. A 1-mm-thick cross-section was removed from the myelinated optic nerve, placed in 4% paraformaldehyde in 0.1M Sorenson's phosphate buffer (pH 7.4), and prepared for axon loss grading as described below.

For serial section studies, the ONH with retina and 1 mm of remaining optic nerve were dissected from the globe and embedded unfixed in optimal cutting temperature embedding media (Sakura Finetek USA, Inc., Torrance CA, USA). Care was taken to orient the blocks for sectioning from the retinal surface to the retrolaminar nerve. Blocks were frozen with dry-ice-chilled 2-methylbutane and stored at −80°C until sectioning.

The ONHs were serially cross-sectioned at a thickness of 10 to 12 µm using a Microm cryostat (HM 500 M Microtome; Microm International GmbH, Walldorf Germany), placing two adjacent sections on each glass slide (Fisherbrand Superfrost Plus; Fisher Scientific, Waltham, MA, USA). Each numbered slide was examined under phase contrast at 10×, and the proportion of the section containing prelamina, the LC, or the retrolaminar optic nerve was noted prior to storage at −80°C. Prelamina was recognized by the absence of connective tissue beams that identify the LC proper. Retrolaminar optic nerve connective tissue beams are more tortuous, and this region was also confirmed by labeling with antibodies against myelin basic protein in some sections (Fig. 1).

Sections were blocked for 30 minutes using 2% normal goat serum or 2% normal donkey serum diluted in PBS with 0.5% Triton X-100 (Sigma-Aldrich, St Louis, MO, USA). Sections were washed and incubated with primary antibodies diluted in the same buffered saline solution overnight at 4°C. Secondary antibodies, phalloidin 568, and 4′,6-diamidino-2-phenylindole (DAPI) were applied for 1 hour at room temperature, then washed in PBS and mounted with Dako mounting media (Agilent, Santa Clara, CA, USA). Antibodies, reagents, and dilutions used are listed in Table 2. Those used for quantitative studies are marked with an asterisk, whereas the remaining antibodies were used for qualitative study.

Confocal and SHG Imaging

Serial cross-sectioned tissues were imaged using a Zeiss LSM 710 NLO system (Carl Zeiss Microscopy LLC, White Plains, NY, USA), outfitted with a Coherent Chameleon Ultra Vision II multiphoton laser (Coherent, Inc., Santa Clara CA, USA). For quantification studies of glial fibrillary acidic protein (GFAP), phalloidin/F-actin, DAPI/nuclei, and collagenous beams, the following acquisition workflow was carried out for each of three to five sections per LC labeled as above. First, a low power confocal roadmap of the entire optic nerve head region was acquired, which typically consisted of a 7 × 7 tile using a Zeiss 20× objective (Plan-Apochromat 20×/0.8 objective) (Fig. 2, Table 3). Second, high-magnification confocal images were acquired as a 2 ×

TABLE 1. Demographic and Clinical Features of Eyes and Persons in LSM Serial Section and TEM Study Groups

Study	Eye	Age, y	Race	Sex	Cup-to-Disc Ratio	Visual Field Outcome	Axon Loss, %
					Glaucoma Serial Section LSM/SHG Study		
1	R	67	E	F	0.9	None	100
2	R	84	E	M	0.4	GHT: ONL, MD −6.8, PSD 6.0, $P = 0.5\%$	0
3	L	84	E	M	0.6	GHT: ONL, MD −11.2, PSD 10.9, $P = 0.5\%$	0
4	R	68	?	?	?	GHT: N, MD −2.5, PSD 1.84, $P = N$	0
5	R	69	?	F	0.3	GHT: N, MD −1.3, PSD 1.9, $P = N$	0
6	R	80	?	?	0.75	GHT: ONL, MD −17.8, PSD 7.9, $P = 0.5\%$	7.5
7	L	80	?	?	0.8	GHT: ONL, MD −14.7, PSD 9.1, $P = 0.5\%$	10
8	L	75	E	M	0.5	None	0
9	R	75	E	M	0.3	None	30
10	L	86	?	?	0.7	GHT: ONL, MD −2.0, PSD 4.5, $P = 2\%$	45
11	R	86	?	?	0.6	GHT: ONL, MD −3.5, PSD 3.2, $P = 5\%$	45
12	R	64	E	M	?	None	25
13	R	72	E	?	0.5	GHT: N, MD −1.0, PSD 3.1, $P = N$	10
14	L	77	?	M	0.6	GHT: ONL, MD −0.02, PSD 1.93, $P = N$	15
15	L	80	E	M	0.9	GHT: ONL, MD −16.8, PSD 11.64, $P = 0.5\%$	50
16	R	88	E	F	0.9	None	80
Summary information ($n = 16$)	10 R, 6 L	75.8 ± 8.0	9 E, 7 ?	7 M, 3 F, 6 ?	0.6 ± 0.2	—	0–100
					Control Serial Section LSM/SHG Study		
1	L	46	E	F	—	—	N/A
2	R	?	?	?	—	—	5
3	R	84	E	M	—	—	N/A
4	L	84	E	M	—	—	N/A
5	L	83	E	F	—	—	0
6	R	83	E	F	—	—	2.5
7	L	68	E	M	—	—	0
8	R	68	E	M	—	—	0
9	L	94	E	F	—	—	0
Summary information ($n = 9$)	4 R, 5 L	75.0 ± 18.7	8 E, 1 ?	4 M, 4 F, 1 ?	—	—	0–5
					Glaucoma Light and TEM Study		
1	R	92	E	F	0.8	GHT: ONL, MD −13.0, PSD 9.5, $P = 0.5\%$	40
2	L	84	E	F	0.85	None	0
3	L	94	E	M	0.7	None	20
4	L	80	E	F	0.9	None	50
5	L	86	E	M	0.8	None	65
6	R	93	?	M	0.4	None	40
7	L	89	E	F	0.6	None	0
8	R	89	E	F	0.6	None	100
9	R	74	E	M	0.5	None	0
10	R	101	E	M	0.3	None	75
11	L	101	E	M	1	None	95
Summary information ($n = 11$)	5 R, 6 L	88.1 ± 8.1	10 E, 1 ?	6 M, 5 F	0.7 ± 0.2	None	0–100
					Control Light and TEM Study		
1	L	96	E	F	—	—	0
2	R	86	E	F	—	—	0
3	R	81	E	M	—	—	0
4	L	83	?	F	—	—	0
5	L	91	E	F	—	—	0
6	L	84	E	F	—	—	0
7	L	98	E	F	—	—	0
8	L	83	E	F	—	—	0
9	R	75	E	F	—	—	0
10	R	98	E	M	—	—	0
Summary information ($n = 10$)	4 R, 6 L	87.5 ± 7.9	10 E, 1 ?	6 M, 5 F	—	—	0

E, European-derived; ?, missing information; F, female; M, male; GHT, glaucoma hemifield test; ONL, outside normal limits; MD, mean deviation (in decibels); PSD, pattern standard deviation (in decibels); *P*, probability value that visual field test exceeded normative values; N, normal; N/A, not available. Summary values for age and cup-to-disc ratio are given as mean ± SD.
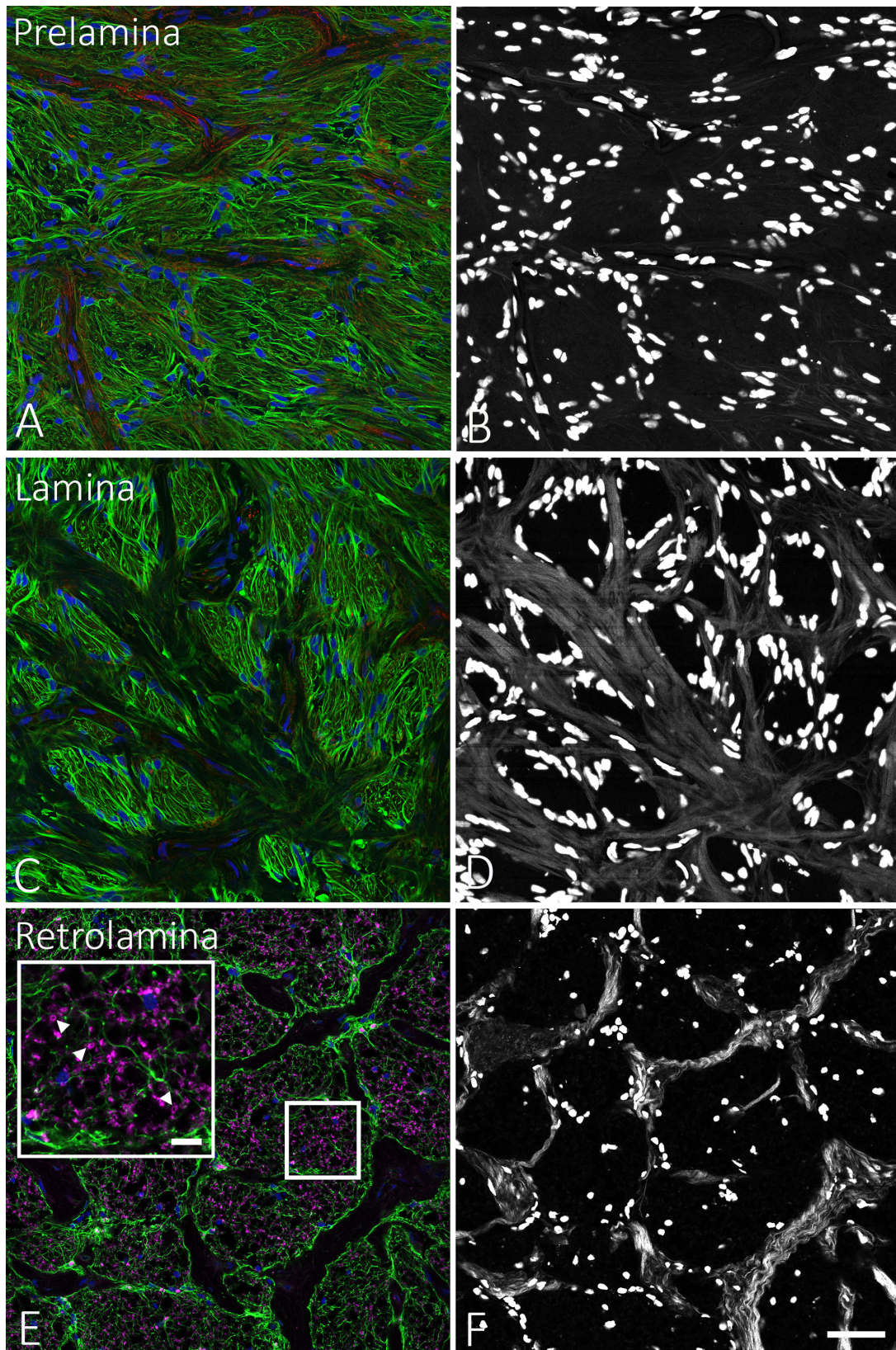
FIGURE 1. Illustration of method used to identify the depth of serial sections that were cut starting in the prelamina, through the LC, to the myelinated optic nerve. (**A**, **B**) Prelamina zone, showing label for GFAP (*green*, **A**) in glial cells but without any white, collagenous beam structures in the SHG image (**B**). (**C, D**) GFAP-positive processes are seen within LC pores (**C**), separated in the LC by collagenous beams seen in the SHG image (**D**). (**E**) In a section that contains some portions in the retrolaminar, myelinated nerve, labeling for myelin basic protein (*purple*) is seen in some pores (box area is shown magnified in larger box with *arrowheads* pointing toward myelin basic protein label). (**F**) In addition, the collagenous beams in myelinated nerve have a thinner and more tortuous structure. *Scale bars*: 50 µm (**A–F**) and 5 µm (**E**, inset).

TABLE 2. Antibodies and Reagents Used in Serial Cross-Section Studies

Primary Antibody	Company	Catalog No.	Species	Dilution	Mono- or Polyclonal
GFAP	Abcam	AB7260*	Rabbit	1:1000	Polyclonal
GFAP	Sigma-Aldrich	AB5541	Chicken	1:500	Polyclonal
IBA1	Wako	019-19741	Rabbit	1:500	Polyclonal
IBA1	Abcam	AB5076	Goat	1:250	Polyclonal
SOX9	Sigma-Aldrich	AB5535	Rabbit	1:500	Polyclonal
TMEM119	Cell Signaling Technology	90840	Rabbit	1: 250	Monoclonal
Collagen IV	SouthernBiotech	1340-01	Goat	1:500	Polyclonal
Myelin basic protein	Abcam	AB7349	Rat	1:1000	Monoclonal

Additional Labels	Company	Catalog No.	Description	Dilution	Excitation Wavelength (nm)
Phalloidin 568	Invitrogen	A12380*	F-actin label	1:70	
DAPI 405	Roche	10-236-276-001*	Nuclear stain	1:1000	

Secondary Antibody	Company	Catalog No.	Species	Dilution	Excitation Wavelength (nm)
Alexa Fluor 488	Invitrogen	A11008	Goat anti-rabbit	1:500	488
Alexa Fluor 488	Invitrogen	A21206	Donkey anti-rabbit	1:500	488
Alexa Fluor 488	Invitrogen	A11055	Donkey anti-goat	1:500	488
Alexa Fluor 568	Invitrogen	A11011	Goat anti-rabbit	1:500	561
Alexa Fluor 568	Invitrogen	A10042	Donkey anti-rabbit	1:500	561
Cy3	Jackson ImmunoResearch	703-165-155	Donkey anti-chicken	1:500	561
Alexa Fluor 647	Invitrogen	A21447	Donkey anti-goat	1:500	633
Alexa Fluor 647	Invitrogen	A21247	Goat anti-rat	1:500	633

Blocking Sera	Company	Catalog No.	Species	Concentration	
Normal goat serum	Jackson ImmunoResearch	005-000-121	Goat	0.5%	
Normal donkey serum	Jackson ImmunoResearch	017-000-001	Donkey	0.5%	

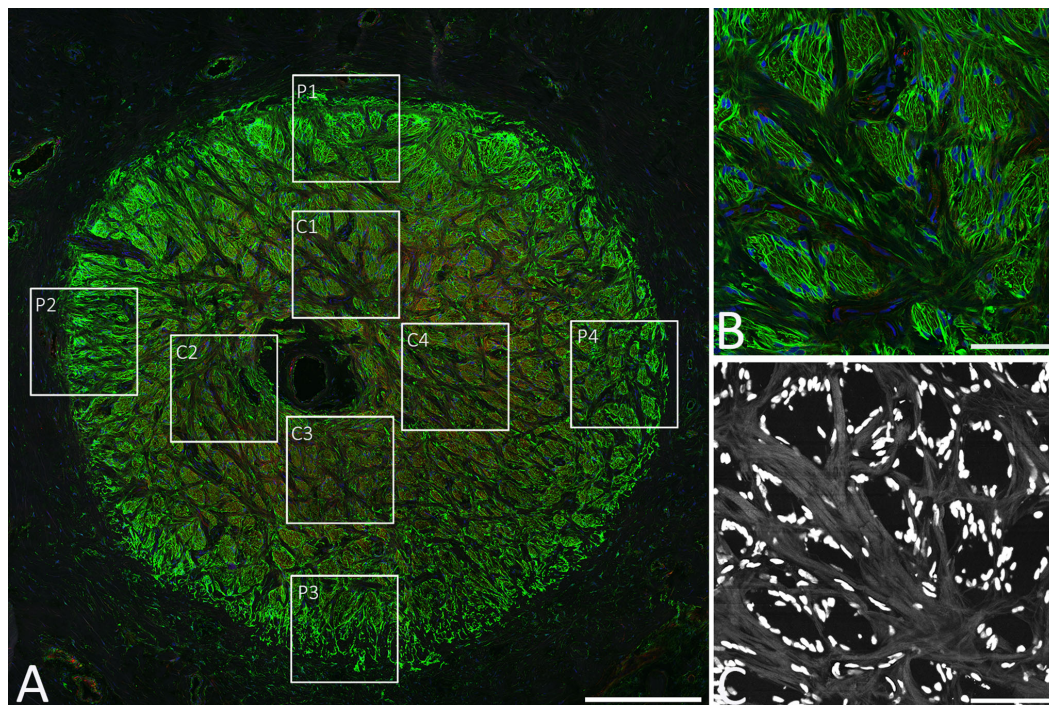*These labels were used for the quantification portion of the study.

FIGURE 2. (**A**) Typical optic nerve LC cross-section labeled for GFAP (*green*), phalloidin/F-actin (*red*), and DAPI (*blue*) that provided a map to locate the eight locations for quantification, four centrally and four peripherally. (**B**) Representative image of GFAP label from a central LC location (region C1 in **A**). (**C**) Second harmonic generation image of region C1 showing beam structure (*gray*) and nuclei (*white*). *Scale bars*: 500 µm (**A**) and 100 µm (**B**, **C**).

2 tile using a 40× objective at 1024 × 1024 resolution and 0% overlap for stitching, resulting in a final image size of 1924 × 1924 pixels, or 399 × 399 µm (Plan-Apochromat 40×/1.3 oil objective). Third, each of the 40× tile loca- tions were immediately reimaged using the SHG modal- ity to visualize the collagenous LC beams and the DAPI- stained nuclei (Table 3). The SHG imaging setup included a multiphoton laser tuned to 790 nm and a 390- to 410-nm

Table 3. Imaging Parameters Used for Quantitative Study

Parameters	Confocal Roadmap	Quantitative Confocal	Quantitative SHG
Objective used	Plan-Apochromat, 20×/0.8 dry	Plan-Apochromat, 40×/1.3 oil	Plan-Apochromat, 40×/1.3 oil
Markers imaged	GFAP/phalloidin/DAPI	GFAP/phalloidin/DAPI	SHG for collagen beams
Number of tiles	7 × 7 = 49	2 × 2 = 4	2 × 2 = 4
Stitched image resolution, pixels	6430 × 6430	1924 × 1924	1924 × 1924
Stitched image size	2.67 × 2.67 mm	399.36 × 399.36 µm	399.36 × 399.36 µm
Stitching overlap, %	12	0	0
Lasers used, nm	405, 488, 561	405, 488, 561	2 photon at 790
Detection wavelengths, nm	410–495, 495–572, 574–712	410–495, 495–572, 574–712	390–410
Averaging used	1	2	1
Pixel dwell time, µs	0.79	1.58	6.3
Slides stained per eye, *n*	3–5	3–5	3–5
Images peripheral (LC/eye), *n*	Not applicable	10–12	10–12
Images central (LC/eye), *n*	Not applicable	10–12	10–12
Total images analyzed per eye, *n*	Not applicable	20–24	20–24

bandpass filter in conjunction with the Zeiss BiG GaAsP detector (a two-channel, gallium–arsenide–phosphide detector). The 40× tile locations were marked on the roadmap as they were collected to avoid overlap and to ensure accurate placement in either the central or peripheral LC regions. In step 2, the laser excitation wavelengths were 488 nm, 561 nm, and 405 nm for Alexa Fluor 488 anti-rabbit GFAP, phalloidin (for F-actin), and DAPI, respectively. The resolution, tiling, and stitching settings were the same for the confocal images of GFAP, phalloidin, and DAPI and for the SHG images to allow for direct comparison during image quantification (Fig. 2, Table 3). To confirm that the regions selected for LC imaging did not include retrolaminar myelinated optic nerve, selected sections were co-labeled with rabbit anti-GFAP, phalloidin, rat anti-myelin basic protein, and DAPI. Astrocyte processes express both GFAP and F-actin, but the analysis of their behavior may be different with the two labeling methods; hence, data from both are included.

Additional antibody labeling was performed using antibodies against IBA1 for microglia and macrophages, TMEM119 for microglia specifically, SOX9 for astrocyte nuclei, and collagen IV to detect basement membranes of astrocytes and capillaries. Confocal and SHG images were captured at either 40× or 63× (Plan-Apochromat 40×/1.3 oil and Plan-Apochromat 63×/1.4 oil) as single-frame images. To quantify the number of astrocytes either within LC pores or lining the edge of pores, an observer (HAQ), masked to the diagnosis of the eye, counted the total number of DAPI-labeled nuclei and the proportion of SOX9 (identifying astrocytes) positive nuclei within pores, as defined by the connective tissue beams visible in the corresponding SHG image. Six glaucoma LC specimens with a variety of axon damage and two controls had counts performed in six sections per LC. SOX9-positive labeling was the presence of multiple punctate bright spots within the nucleus and a rim of positivity around the nuclear envelope. Although labeling for microglia was seen in processes within the LC pores, these could not be identified as belonging to particular cell nuclei. We therefore reported the percentage of nuclei positive for nuclear SOX9 labeling and assumed that nuclei that were SOX9 negative represented other cell types.

Quantification of Serial Section Data

Structural characterization was performed on cross-section confocal and SHG images using a semi-automatic method based on the method by Ling et al.[44,51] Four main structural features were used for analysis: the GFAP label, the F-actin (phalloidin) label, the DAPI label (nuclei), and the SHG image (beam structure). A total of 46 structural parameters (Table 4) were measured using the stated code in MATLAB R2019a (MathWorks, Inc., Natick, MA, USA). The F-actin and GFAP images were processed with a median filter to reduce noise and with contrast-limited adaptive histogram equalization to brighten dim features. The enhanced images were separately binarized, with F-actin, GFAP, and nuclei labeled in white and the background pixels in black. The segmented GFAP and F-actin structures were combined to create a two-dimensional image of the LC with distinct areas of GFAP, F-actin, overlapping GFAP and F-actin, and axonal compartments. The axonal compartments were defined as areas not labeled for GFAP or F-actin within each LC pore boundary. An optic nerve boundary was marked at its periphery to include only LC within the PPS, as the four peripheral LC sampled images for each nerve section included the outermost pores in some portion of the image. The image processing and structural measurement code is published.[52] The SHG images were similarly processed to quantify the connective tissue beam structure of the LC. The images were binarized into pores and beams, with beams appearing in SHG images as bright reflective zones indicative of collagen fibers (Fig. 3).

Area fraction was the proportion of the stated image component area (only within pores, within beams, or overall) occupied by the structure. Process widths were calculated from each binarized image after it was skeletonized using the MATLAB function 'bwmorph' with options 'thin' and 'inf.' Skeletonization created a network of 1-pixel-wide curves tracing the midline of each process. Process width at each skeleton pixel was measured as two times the shortest distance from the skeleton pixel to the process boundary. The aspect ratio of nuclei quantified the difference in shape from perfectly round to oblong. Axon compartments were judged to be those areas within pores not labeled by anti-GFAP antibodies, phalloidin, or DAPI.

Light and TEM Study Methods

Eyes for the light and TEM study group were fixed with 4% paraformaldehyde in 0.1-M Sorenson's phosphate buffer (pH 7.4). For the estimation of RGC axon loss, a 1-mm-thick segment of the myelinated optic nerve was removed and

TABLE 4. Quantified Parameters of ONH Components

Tissue Component	Structural Parameter
GFAP in pores	Area fraction
	Mean ± SD of process width
	Maximum process width
GFAP overall	Area fraction
	Mean ± SD of process width
	Maximum process width
F-actin in pores	Area fraction
	Mean ± SD of process width
	Maximum process width
F-actin overall	Area fraction (F-actin area/mask area)
	Mean ± SD of process width
	Maximum process width
Beam structure (SHG)	Area fraction
	Mean ± SD of beam width
	Maximum beam width
Pore area (negative SHG space)	Mean ± SD area of pores
Nuclei overall	Total nuclear area
	Median of nuclear area
	Mean ± SD of nuclear area
	Median aspect ratio of nuclei
	Mean ± SD of aspect ratio of nuclei
	Count of nuclei
	Percentage of nuclei overall
	Area percentage of nuclei overall
Nuclei in pores	Total nuclear area
	Median of nuclear area
	Mean ± SD of nuclear area
	Median aspect ratio of nuclei
	Mean ± SD of aspect ratio of nuclei
	Count of nuclei
	Count/area
	Percentage of nuclei in pores
	Area percentage of nuclei in pores
Nuclei on beams	Total nuclear area
	Median of nuclear area
	Mean ± SD of nuclear area
	Median aspect ratio of nuclei
	Mean ± SD of aspect ratio of nuclei
	Count of nuclei
	Count/area
	Percentage of nuclei on beams
	Area percentage of nuclei on beams
Axonal compartments	Number of axonal compartments
	Total axonal area
	Median of axonal area
	Mean ± SD of axonal area

Linear measures were expressed in units of μm and areas in μm^2.

processed. The entire ONH, including the LC and the PPS, was removed from the eye and separated from the choroid and retina. Each was cut longitudinally in half. Tissue was post-fixed in 1% osmium tetroxide, dehydrated in ascending alcohol concentrations, and stained in 1% uranyl acetate in 100% ethanol for 1 hour. The specimens were embedded in epoxy resin at 60°C for 48 hours. Sections 1 μm thick were cut with glass knives using a Leica UC7 ultramicrotome (Leica Microsystems, Wetzlar, Germany), and stained with 1% toluidine blue. Images of the optic nerve cross-section were taken with the ACCU-SlideMS Manual Slide Scanning System (ACCU-SCOPE, Commack, NY, USA). Ultra-thin sections (~68 nm) were collected on copper grids using a diamond knife and the Leica UC7 ultramicrotome, then stained with uranyl acetate and lead citrate prior to examination with a Hitachi H-7600 Transmission Electron Microscope (Hitachi High-Tech America, Inc., Gaithersburg, MD, USA).

Masked Grading of Optic Nerve Cross Sections

Myelinated optic nerve cross-sections were embedded in epoxy as above and thick sections cut at 1 μm with 1% toluidine blue staining. Identification numbers for the nerves were masked. Two observers (HAQ and TVJ) independently graded the nerves for damage to the nearest 5% on a scale from 0% (normal) to 100% (total loss) (Fig. 4). The gradings of the two observers were averaged to derive the percentage of damage for each nerve. If the difference between the two observer's damage values was greater than 15%, the nerve grading was adjudicated by the two observers. Adjudication was needed in 10 of 56 nerves graded for the study.

Statistical Analyses

Statistical analyses were performed on the quantitative parameters of the F-actin, GFAP, DAPI, and beam structures. In addition to the finding for the three sections of each LC, we compared the central four images to the peripheral four images from each LC, and we compared values between the overall control group and the overall glaucoma group. We also compared the glaucoma eyes by degree of axon loss. Three-level linear mixed-effect (LME) models with random intercept (participant and eye) were used to compare glaucoma versus control, peripheral versus control, and the association between each LC and degree of damage among glaucoma patients (using R; R Foundation for Statistical Computing, Vienna, Austria). In all models, age and sex were tested as potential co-variates. For each LC, univariate LME modeling was performed on glaucoma versus control, peripheral versus central, and demographics, followed by multivariate LME modeling on glaucoma versus control and peripheral versus central. Similarly, univariate analyses followed by multivariate analyses were performed on degree of damage and peripheral versus central among the glaucoma group and peripheral versus central among the control group. Regression models were applied to the glaucoma LCs in order to account for the degree of estimated axonal loss in the optic nerve tissue sections. Each univariable or multivariable LME analysis accounted for the internal correlations produced by the inclusion in some cases of both eyes of an individual, as well as the correlation produced for each LC parameter by the inclusion of three sections to generate the mean or median value for a parameter for that LC. Univariable parameters that were significant at $P < 0.15$ were entered into the models, and parameters that had $P < 0.05$ were considered significant. As indicated in the Results section, for some comparisons, analysis of variance was used where appropriate, as were *t*-tests for normally distributed parameters.
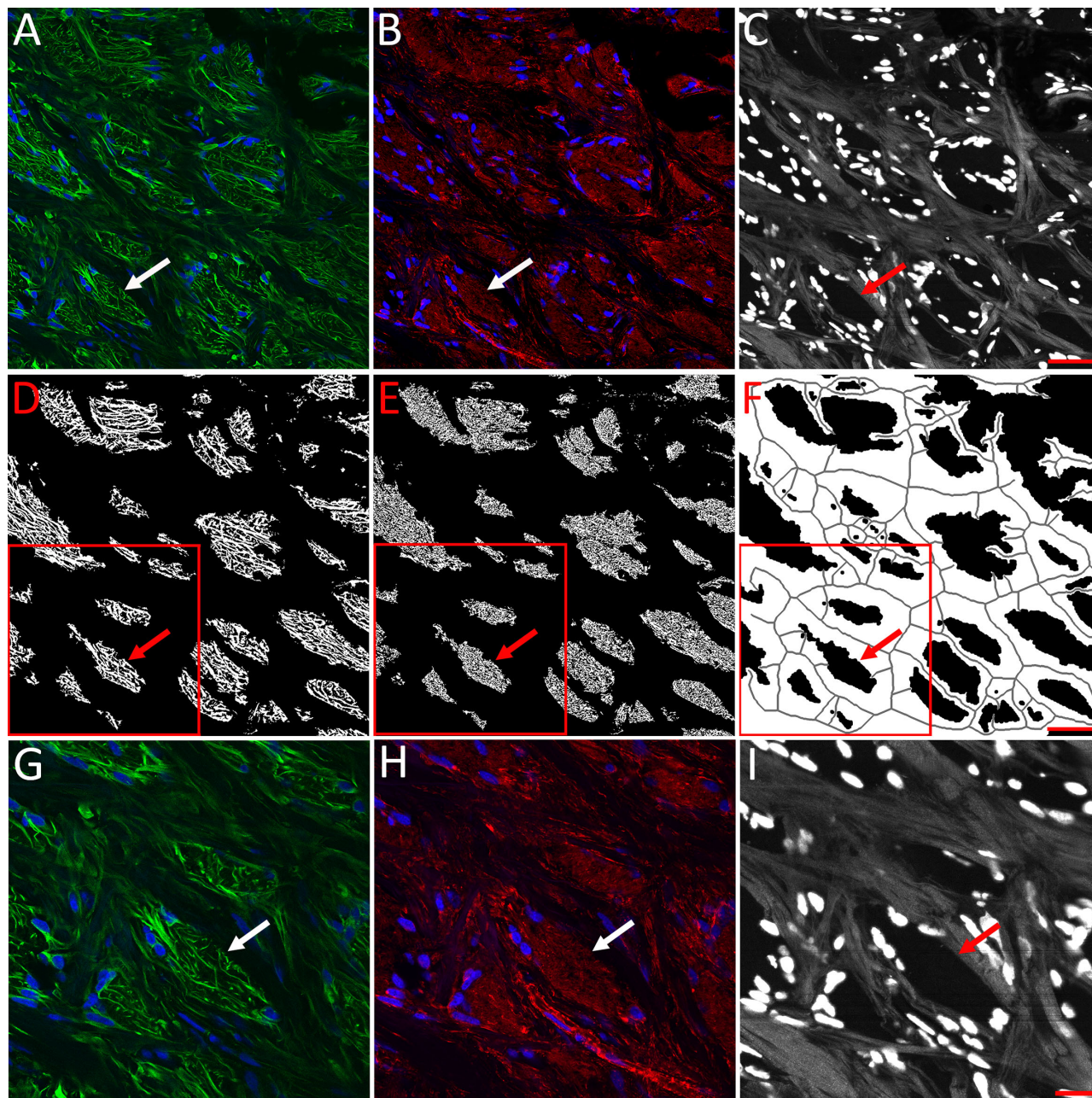
FIGURE 3. (**A–C**) Example of a control image from the LC used for analysis with labeling of GFAP (*green*) and DAPI (*blue*) (**A**), F-actin (*red*) and DAPI (*blue*) (**B**), and beams of LC (*gray*) and nuclei (*white*) by SHG imaging (**C**). (**D–F**): Binary analysis used to measure process structures within LC pores (**D**, **E**) and beam structure (**F**). (**G–I**) Individual higher power images from **A** to **C** (*red box area*) that show greater detail within boxed areas. *Arrows* (*white and* red) point to the same LC pore location in each image. *Scale bars*: 50 μm (**A–F**) and 20 μm (**G–I**).

RESULTS

Control Structural Features

Within the pores of the control LC tissue, the area fraction of GFAP-labeled processes was 50.9% ± 3.7% of pore area, and the area fraction of F-actin–labeled astrocyte processes was similar at 48.1% ± 2.8% (Table 5, Fig. 5). The mean width for GFAP-labeled processes was substantially larger than that of F-actin–labeled processes. It was not possible to determine whether this was due to an actual difference in the distribution of intermediate filaments (GFAP-containing) and F-actin fibers or, alternatively, was due to differences in the image processing methods. The median LC connective tissue beam width was 10.6 μm, and the median of the maximum beam width was 51 μm. The median diameter of pores (the spaces between SHG-identified beams) was 41 μm. The median axon compartment area was 0.64 μm^2 with a mean area of 3.7 ± 17 μm^2. The typical human RGC unmyelinated axon is <1 μm in diameter; thus, this mean area would comprise about one axon in cross-section, whereas the size of the variance suggests that groups of axons were counted together as one axon compartment.
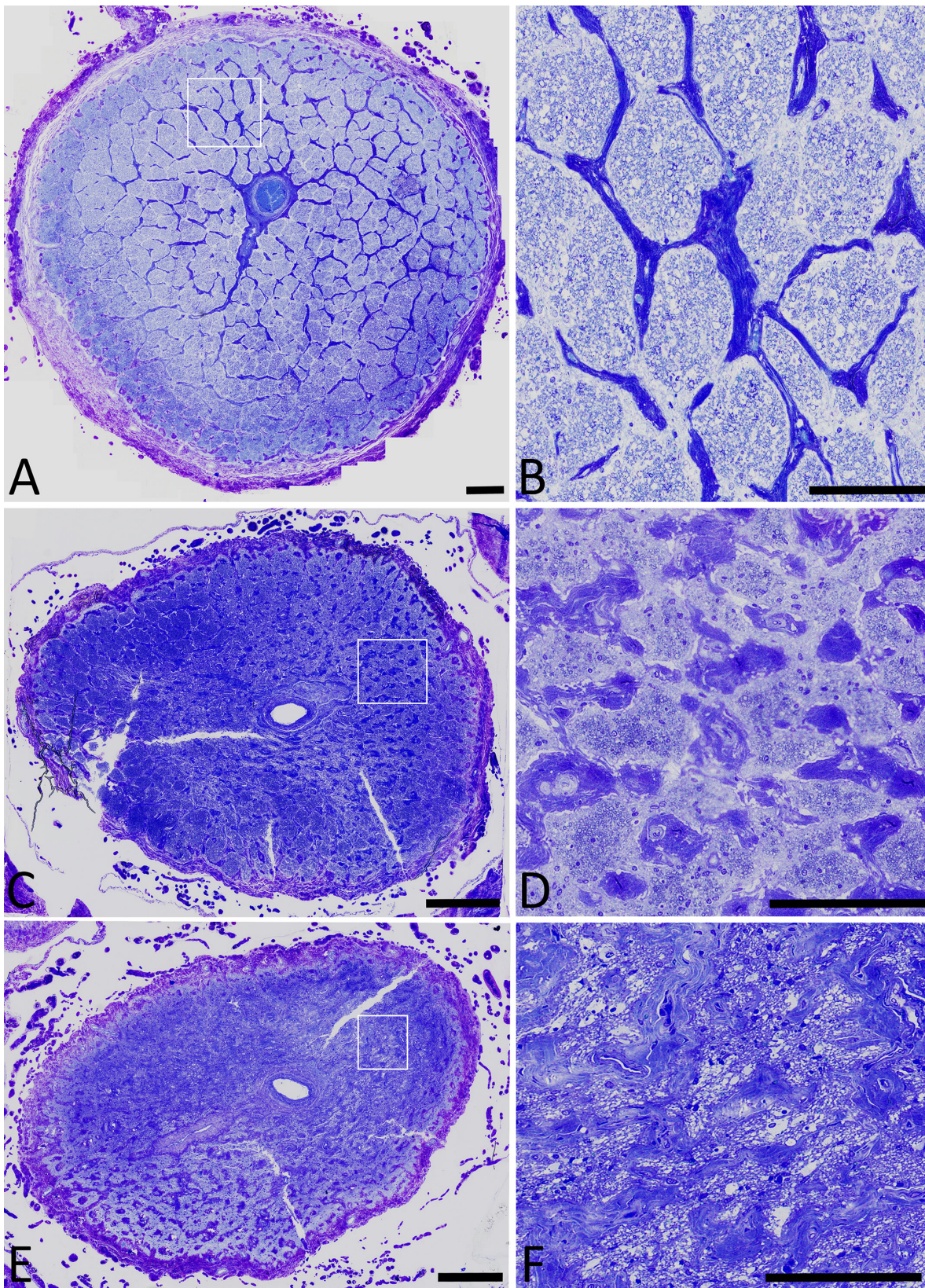
Figure 4. Cross-sections of three nerves from the myelinated optic nerve, illustrating the damage grading method. (**A**) Normal nerve (graded 0% loss). (**B**) Higher power image of boxed region in **A**, showing a normal complement of axons in nerve bundles. (**C**) Nerve with a substantial loss of axons and narrowing of bundles (graded 60% loss). (**D**) Higher power of **C** showing major loss of axons with narrowing of axon bundles. (**E**) Nerve with severe damage (graded 95% loss). (**F**) Higher power of **E** showing no remaining axons, with *clear circles* representing macrophages with phagocytosed axons. *Scale bars*: 100 µm (**A**, **C**, **E**) and 50 µm (**B**, **D**, **F**).

TABLE 5. Comparison of Selected Structural Parameters Between Control and Glaucoma LC

Tissue Component	Structural Parameter	Mean ± SD		P
		Control ($n = 9$)	Glaucoma ($n = 16$)	
GFAP in pores	Area fraction (GFAP area/mask area)	0.51 ± 0.04	0.48 ± 0.03	0.01*
	Average process width (μm)	1.60 ± 0.10	1.63 ± 0.09	0.42
F-actin in pores	Area fraction (F-actin area/mask area)	0.48 ± 0.03	0.44 ± 0.04	0.07
	Average process width (μm)	1.05 ± 0.03	1.07 ± 0.08	0.28
Nuclei overall	Median aspect ratio of nuclei	2.04 ± 0.20	1.88 ± 0.13	0.02*
Axon compartments	Median of axonal area (μm^2)	0.64 ± 0.04	0.58 ± 0.07	0.05*

* Indicates significant *P* values from multivariable linear mixed-effect models.

Control Compared to Glaucoma Structural Features

Within pores, the area fraction of both GFAP processes was significantly lower in glaucoma eyes overall than in controls (Table 5, Fig. 5). The area fraction of F-actin processes was significantly lower in the univariable model ($P = 0.025$) but did not achieve the $P = 0.05$ level in multivariable analysis. The GFAP and F-actin area fraction overall, including both the beams and the pores, did not differ significantly between glaucoma and non-glaucoma eyes (Supplementary Table S1). Likewise, there was no significant difference in GFAP or F-actin process width within pores between glaucoma and control LC. Second, there was a significantly lower median aspect ratio of nuclei in glaucoma compared to control LC, with the nuclei in control eyes appearing twice as long as they were wide in contrast to nuclei in glaucoma eyes which were rounder (lower aspect ratio). Third, the medians of axonal compartment area and total compartment area were significantly lower in glaucoma eyes (Table 5). None of the other parameters significantly differed between control and glaucoma in LME models. However, the glaucoma group had a diversity of damage, from none to severe, with eight of the eyes with clear glaucoma history having minimal axon loss in their optic nerve cross-section (Table 1). We next compared the glaucoma eyes alone by degree of damage.

Glaucoma Findings by Degree of Damage

In LME models that assessed the effect of the degree of glaucoma damage, there were several parameters that differed by injury level (Table 6). The F-actin process width both within pores and overall was significantly wider in glaucoma eyes as damage increased. Average LC beam width decreased significantly with increasing glaucoma damage. Within pores among glaucoma eyes, nuclear count per square millimeter increased with increasing damage, but the same was not true for nuclei associated with LC beams. The number of axonal compartments tended to decrease with increasing glaucoma damage in a model that also indicated that glaucoma eyes had fewer axons in peripheral regions than centrally and fewer with increasing age. Parameters that did not differ by degree of glaucoma damage included GFAP and F-actin area fraction, area fraction of GFAP and F-actin within pores, and beam area fraction. Slope and *P* values were calculated from multivariable LME models. A positive slope indicates the amount that value increased with each 1% worse glaucoma damage. A negative slope indicates that the value declined with worse damage.

Differences Between Central and Peripheral LC Regions

For control eyes, the GFAP area fraction in peripheral pores was greater than centrally, and the mean GFAP and F-actin process widths were larger in peripheral pores (Table 7). The mean area of pores was smaller in the peripheral LC. However, the number of nuclei per area (density) was lower within beams in the peripheral LC, and the density and area of nuclei were higher in central pores (Table 7). The number of axonal compartments was lower in the peripheral LC.

The comparison of central to peripheral features in the overall glaucoma group followed many of the same trends seen in the control eyes (Table 7). However, controls had smaller pore areas in the periphery, and glaucoma eyes had equal areas of pores between central and peripheral zones. Furthermore, controls had more pore nuclei and a higher percentage of pore nuclei area in peripheral than in central pores, but this difference was less or reversed in glaucoma eyes.

Light Microscopy, TEM, and Additional Immunohistochemical Data

In the serial cross-section data above, glaucoma eyes with greater damage had significantly more nuclei within the pores, thinner beam width, and wider F-actin–labeled cell processes. In addition, the number of axonal compartments declined with greater optic nerve axon loss; yet, the amount of axon compartment decrease was less than the estimated axon loss from myelinated optic nerve assessment. We investigated further the composition of the LC pores and the definition of axon compartments by additional immunohistochemical labeling and TEM studies of additional control and glaucoma eyes listed in Table 1.

In the light microscopic sections, glaucoma eyes had more nuclei in longitudinally sectioned axonal bundles passing through the LC than did control eyes (Fig. 6). The number of nuclei within pores (between beams) was greater in glaucoma LC and greatest with severe axon loss, as estimated from the optic nerve cross-sections in the same eyes. To identify the cell types whose nuclei were more prevalent in LC pores in glaucoma eyes, we labeled selected cross-sections of LC for SOX9 (a nuclear marker identifying astrocytes) (Fig. 7), for IBA1 (microglia/macrophage processes) (Fig. 8), and for TMEM119 (specific for microglial processes) (Supplementary Fig. S1). In two control LCs, 97% of nuclei were SOX9 positive in masked grading. In six glaucoma eyes (Table 8), 92.3% of nuclei were SOX9 positive. The SOX9-negative nuclei were smaller and rounder than the positive
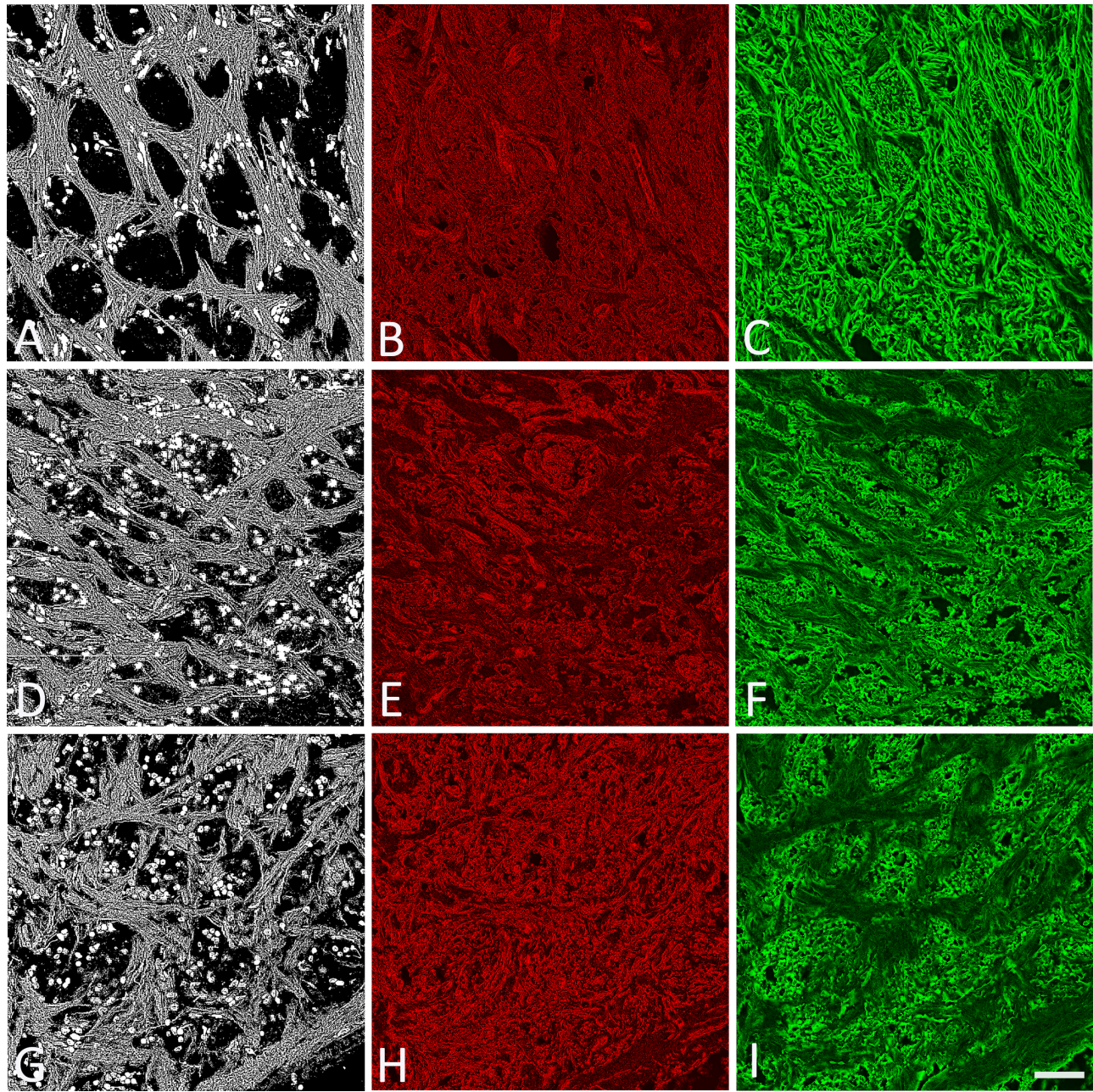
FIGURE 5. Control (**A–C**) and glaucoma (**D–H**) LC, imaged by SHG (**A**, **D**, **G**) and with labels for F-actin (**B**, **E**, **H**) and GFAP (**C**, **F**, **I**). Compared to control (**A–C**), the examples with moderate glaucoma damage (**D–F**) and severe glaucoma damage (**G–I**) show nuclei more prevalent in pores (*white ovals* in left column images). In addition, the pattern of F-actin and GFAP labeling is changed in the moderate and severe glaucoma specimens. *Scale bar*: 50 μm.

TABLE 6. Structural Parameters by Degree of Glaucoma Damage

Tissue Component	Structural Parameter	Slope (±SE)	*P*
F-actin in pores	Average process width, μm	0.0014 ± 0.00042	0.041
F-actin overall	Average process width, μm	0.0014 ± 0.00040	0.042
Beam structure	Average beam width, μm	-0.027 ± 0.0081	0.042
Nuclei in pores	Count $\times 10^3$/mask area, n/μm^2	0.0000070 ± 0.0000015	0.019
Axon compartments	Axonal compartments, n	-64.4 ± 20.7	0.053

nuclei. Thus, the major cell type in both control and glaucoma LC pores were astrocytes. Some cell processes were positively labeled for IBA1 and/or TMEM119, suggesting that some SOX9-negative cells were microglia. None of the SOX9 negative nuclei had the morphology of fibroblasts or endothelial cells, whose nuclei are typically more oblong.

TABLE 7. Comparison of Central to Peripheral LC Zone Structural Parameters in Control and Glaucoma

Tissue Component	Structural Parameter	Percent Difference Peripheral Over Central (%)			
		Control	*P*	Glaucoma	*P*
GFAP in pores	Area fraction, GFAP area/mask area	4.9	0.0008[*]	4.2	0.011[*]
	Average process width, µm	2.9	0.005[*]	2.3	0.029[*]
F-actin in pores	Area fraction, F-actin area/mask area	1.1	0.402	3.4	0.044[*]
	Average process width, µm	3.9	2.34E-08[*]	2.1	0.001[*]
Beams (SHG)	Mean area of pores, µm^2	−18.2	0.022[*]	−5.4	0.415
Nuclei overall	Count × 10^3/mask area, n/µm^2	−23.6	0.251	−5.4	0.012[*]
Nuclei in pores	Count × 10^3/mask area, n/µm^2	10.3	0.059	−8.5	0.041[*]
	Area percentage of nuclei in pores	21.5	0.007[*]	6.6	0.092
Nuclei on beams	Count × 10^3/mask area, n/µm^2	−14.2	0.007[*]	−4.6	0.133
Axon compartments	Number of axonal compartments	−19.0	1.34E-09[*]	−11.5	3.11E-05[*]

[*] Indicates significant *P* values from multivariable linear mixed-effect models.

TABLE 8. Number of SOX9-Positive Nuclei Within LC Pores

Total Nuclei Counted, *n*	Axon Loss (%)	Astrocytes (%)	Status
78	0	97.7	Control
61	0	97.2	Control
54	5	87.3	Glaucoma
114	15	94.7	Glaucoma
73	25	99.0	Glaucoma
23	30	56.1	Glaucoma
158	45	93.7	Glaucoma
177	50	93.0	Glaucoma

In TEM examinations of five glaucoma eyes with various levels of damage, we found that within the LC pores there were many processes of astrocytes identifiable by their typical intermediate filaments (which are known to consist of GFAP, vimentin, and nestin). Adjacent to these astrocytes, in the middle of pores, there was basement membrane material (Fig. 9), which in normal LCs is present only between astrocytes and the connective tissue beams (or within beams associated with capillaries), but not in mid-pore regions. In addition, there were fibrils typical for collagens I and III that are not found within pores.[27] This material, due to both its structure and its random orientation, does not show brightly in SHG images and thus would be interpreted in our analytic framework as "axon compartments." To confirm further that the material that we identified by electron microscopy was basement membrane within pores, we labeled some serial cross-sections of LC for collagen IV, a major component of basement membrane. Control LC had no collagen IV labeling within pores, but glaucoma eyes had extensive collagen IV labeling inside pores (Fig. 10).

DISCUSSION

There have been few quantitative reports of disease-related changes in the human LC in open-angle glaucoma (OAG). Some investigations of non-human primate models of glaucoma have provided quantitative data. In this report, we utilized only eyes in which a detailed clinical history of OAG care was obtained, many with visual field testing and all with quantification of the degree of optic nerve axon loss by histological assessment. It is vital to confirm the degree of axon damage, as our statistical models demonstrated important differences in astrocyte and beam alteration that were evident when the data were analyzed by degree of injury, compared to contrasting all OAG eyes against controls. Many studies of the glaucomatous nerve head tissues refer only to "glaucoma" eyes, but doing so ignores the likely differences among them in stage of damage.

In both human glaucoma eyes[3] and monkey experimental glaucoma,[52,53] as axon loss occurs astrocytes move into LC pores, producing matrix materials, such as collagens I, III, and IV. This also occurs in a rat glaucoma model, despite the lack of collagenous beams or LC fibroblasts, where astrocytes deposit collagens I, III, IV, and VI along with chondroitin and dermatan sulfate proteoglycans within axon bundles.[54] Astrocytes alter their synthetic phenotype, degrade matrix, phagocytose axonal debris, likely synthesize collagen IV, and actively divide in human glaucoma ONH, appearing to increase their presence within LC pores.[55] In this study, we determined that astrocytes move from positions on LC beams into the pores, aligning anteroposteriorly, as has also been observed in rodent glaucoma models.[56] The change in nuclear aspect ratio toward rounder rather than oval nuclei is compatible with this reorientation. Our data show that the increase in astrocyte nuclei within LC pores was greater in glaucoma eyes with more damage. Yet, within LC pores in glaucoma eyes, GFAP and F-actin area fractions were significantly lower than in controls. There are several potential explanations for these findings. First, astrocytes may reduce their GFAP production as part of a reactive change. Interestingly, this would be the opposite of astrocyte reactivity in the brain, where astrocyte reaction is characterized by change from minimal to elevated GFAP production. Second, the reorientation of astrocyte processes from the plane of our serial cross-sections toward perpendicular to it may reduce the visibility of processes. Third, axons are removed by astrocytic phagocytosis,[3] changing the labeling characteristics of the astrocytes. Fourth, the increase in nuclei within pores may represent proliferation of non-astrocytic cells, most likely microglia/macrophages. We have demonstrated proliferation of both astrocytes and microglia in a mouse glaucoma model[37]; however, we determined that more than 90% of cell nuclei in human glaucoma LC pores belong to astrocytes. Finally, the non-astrocytic space formerly occupied by axons may now consist of a greater proportion of newly synthesized matrix, including collagen IV and other collagens.

The normal configuration of astrocytes of the LC in humans and in rodents that lack connective tissue within the LC anchors the astrocyte at its junction with connective tissues by synthesis of basement membrane and construction of specialized junctional complexes on the
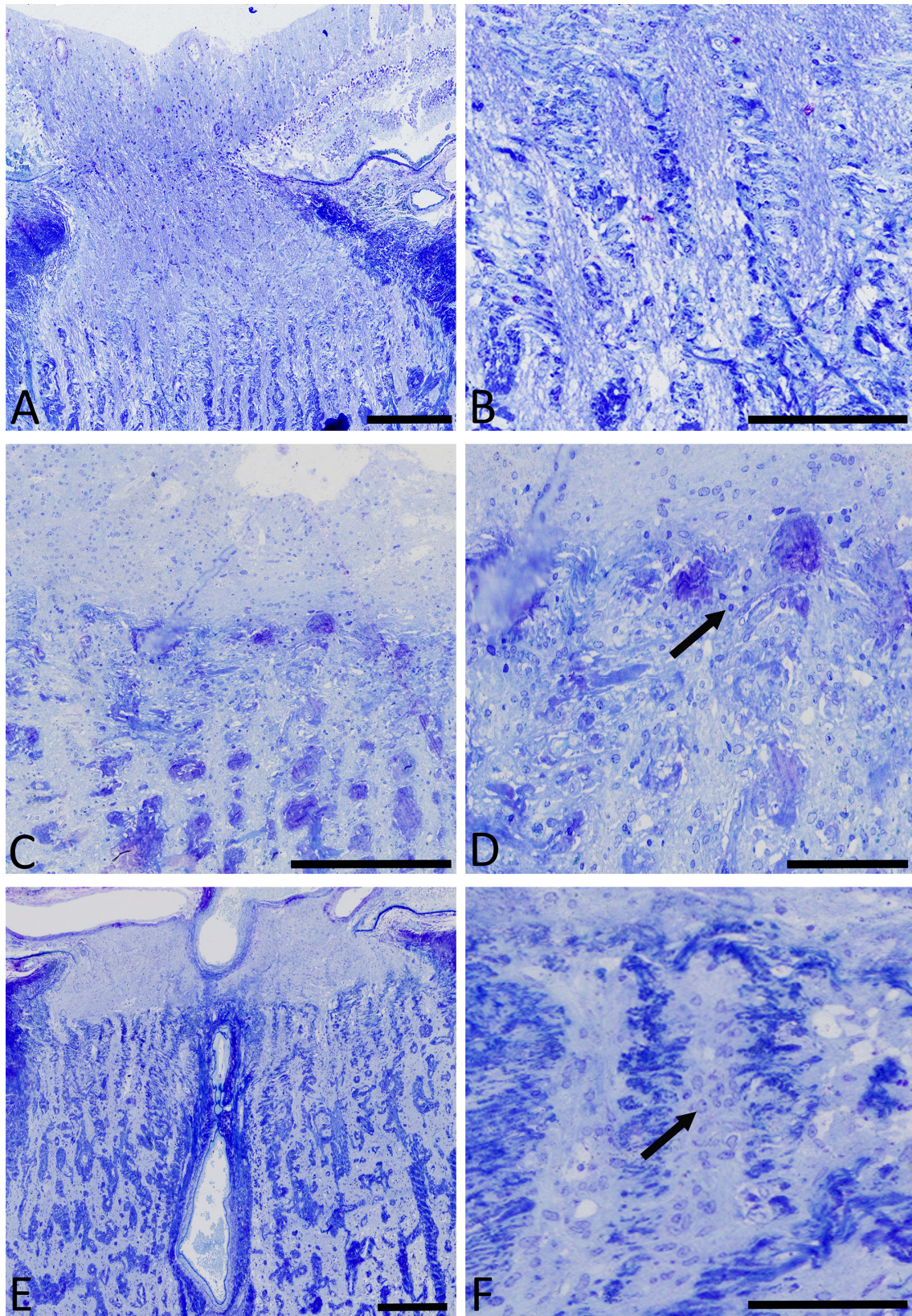
FIGURE 6. Longitudinal epoxy sections of human optic nerve stained with 1% toluidine blue. (**A**) Normal nerve graded as 0% damage with nuclei (*blue ovals*) lining the connective tissue beams in orderly columns. (**B**) Higher magnification showing nuclei on beams but not within pores in the LC. (**C**, **D**) Moderate damage glaucoma eye (60% loss) with reduced axons and nuclei more often within bundles (*arrow*). (**E**, **F**) Severe damage (100% loss with nuclei filling pores, *arrow*). *Scale bars*: 100 µm (**A**, **C**, **E**) and 50 µm (**B**, **D**, **F**).
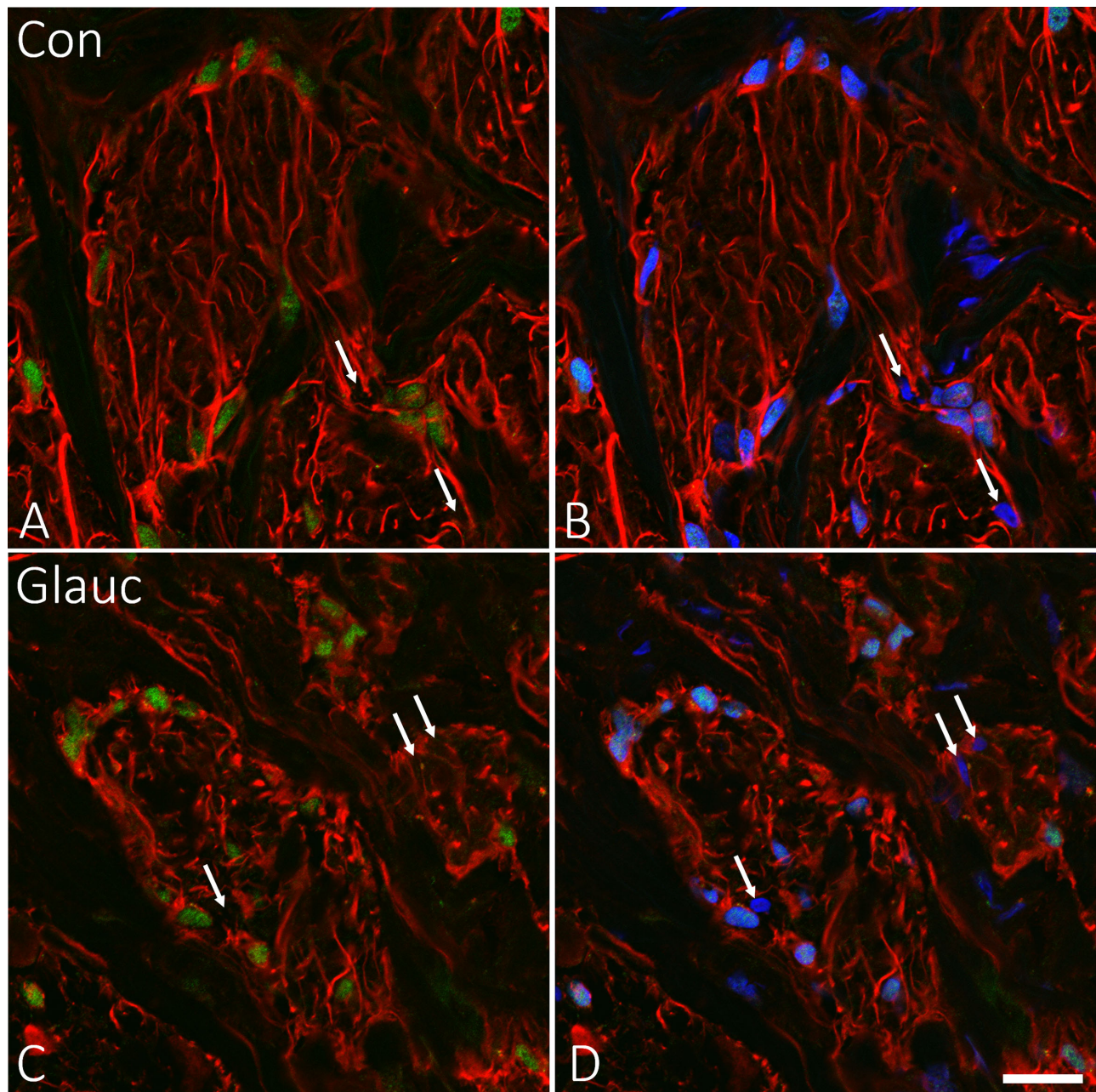
Figure 7. SOX9 labeling of nuclei in control (**A**, **B**) and glaucoma (**C**, **D**) LC. GFAP (*red*; **A–D**), SOX9 (*green*; **A**, **C**) and DAPI (*blue*; **B**, **D**). In both control and glaucoma, most nuclei are SOX9-positive astrocytes. Approximately 10% of DAPI-labeled nuclei are not labeled with SOX9 (*arrows*) and represent other cell types. *Scale bar*: 20 μm.

internal cell border.[37] These junctional complexes are also found in astrocytes of pig and human LC astrocytes (data not shown). In a mouse glaucoma model, IOP-generated stress on LC astrocytes causes alteration in the transmembrane linkage to the sclera via its basement membrane and disconnection of the junctional complexes, with concomitant increase in biomechanical strain.[57] The effect is simulated by treatment of the mouse eye with trypsin, which both causes such disconnection and increases strain.[58] Our findings confirm in human OAG the reports from rat and monkey glaucoma models that astrocytes migrating into axonal bundles (pores) produce collagens at locations that are aberrant.

In human postmortem glaucoma eyes, the canal opening at Bruch's membrane does not widen, but the LC behind it widens, expanding beyond the Bruch's membrane opening to produce the clinical appearance known as excavation.[59] The Gaussian, mean, and minimum curvatures of the anterior border of the LC increase,[60] and there is compression of the successive LC plates, indicating that initial compressive strains become fixed in the remodeling process. LC beams in non-human primate and human ONH have fibrils of collagens I, III, and V, and collagen IV and laminin comprise the basement membranes of astrocytes that normally separate the beam matrix from axons.[61] Glycosaminoglycans, including chondroitin sulfate, dermatan sulfate, and heparan
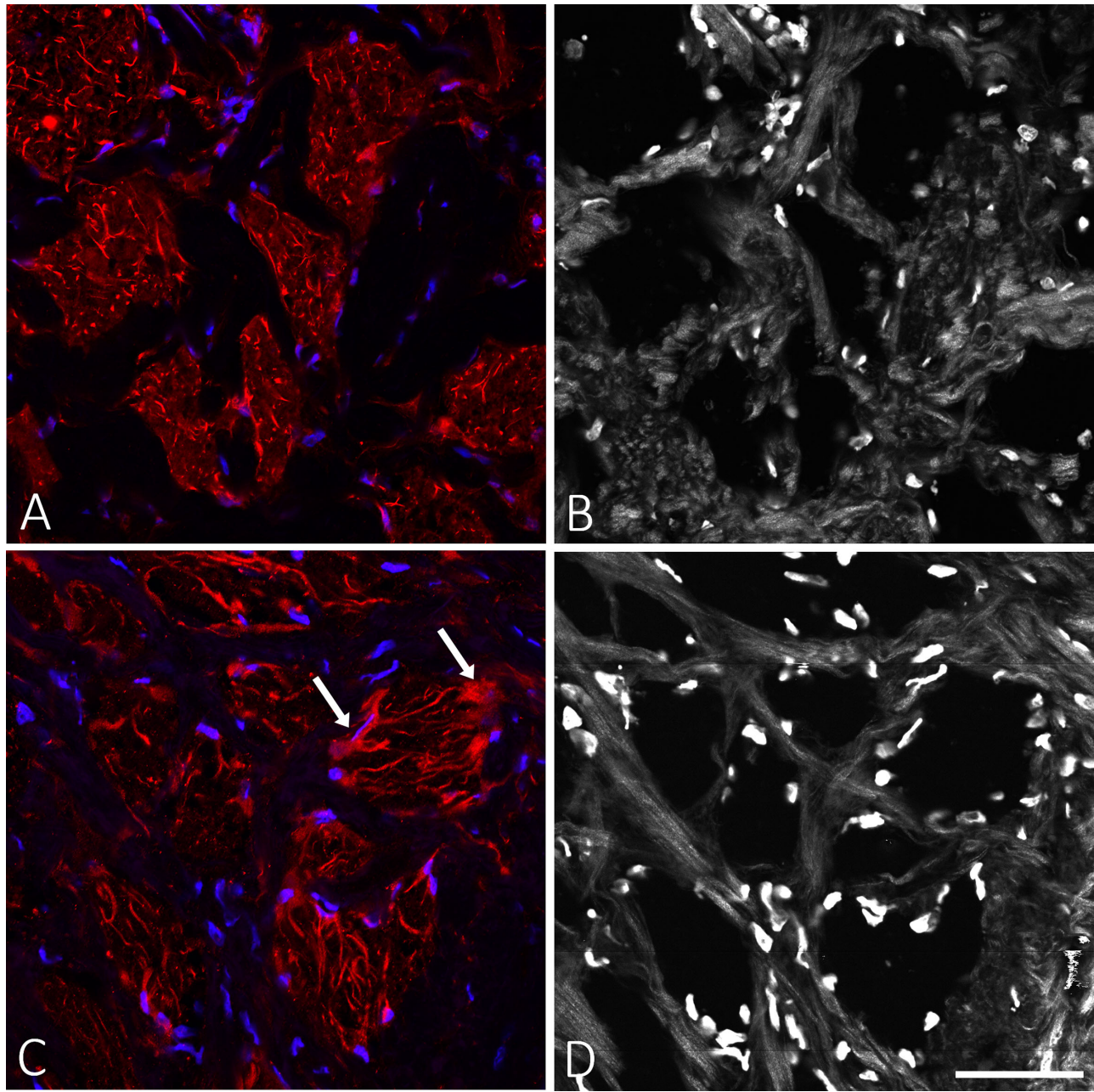
FIGURE 8. (**A**) Control eye LC stained with IBA1 (*red*) and DAPI (*blue*). (**B**) Same area imaged with SHG. (**C**) LC from glaucoma eye with 30% axon loss labeled with IBA1 (*red*) and DAPI (*blue*). (**D**) SHG image of area in **C**. Presumed microglial or macrophage processes (IBA1+) are more prominent in the glaucoma example (*arrows*). *Scale bar*: 50 µm.

sulfate, are non-fibrous beam elements.[62] There are changes in the LC beam composition with age, including an increase in elastin and a decrease in fibronectin and glycosaminoglycans, but the number of cells after 60 years of age remains stable.[63] In glaucomatous nerve heads, LC beams undergo a decrease in collagen density without a change in fibril diameter distribution or in elastin density, whereas elastin fibrils are substantially more crimped in glaucoma beams.[28] Consistent with this finding, our present data show that LC beam width was significantly thinner in glaucoma eyes with greater damage. The PPS undergoes a similar decrease in collagen density in glaucoma.[64] We previously found no quantitative difference between control and glaucomatous

eyes in elastin content or its ultrastructure between control and glaucomatous eyes.[65] Data from en face images of the ONH in adaptive-optics optical coherence tomography (AO-OCT) found, as we did with tissue sections, that pore area, pore count, and pore density were not different in glaucoma and control ONH.[66] However, in our study of LC of unfixed eyes with SHG imaging, glaucoma eyes exhibited a smaller average pore area, greater beam tortuosity, and a more isotropic beam structure than the LC of normal eyes.

In order to build appropriate models of ONH behavior in glaucoma, detailed anatomical and physiological data on actual human glaucoma eyes are needed. In human eyes with glaucoma, the mechanical properties of the
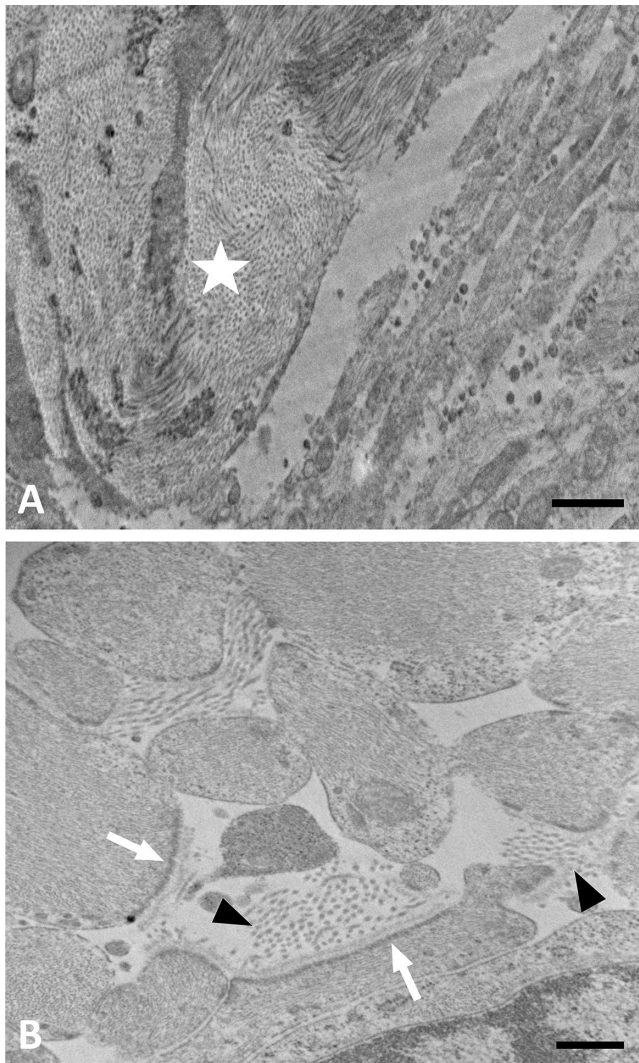
FIGURE 9. TEM image of LC pore remodeling in a glaucoma. (**A**) Lower magnification of moderately damaged glaucoma ONH showing lamina beam (*star*) with collagen and elastin. Pore area at *lower right* shows many astrocyte processes. (**B**) Higher power of pore area has astrocyte processes with expanded extracellular space, containing collagen fibrils (*arrowheads*). Astrocytes have incomplete basement membrane with dense junctional complexes facing only those areas where basement membrane is present (*white arrows*). *Scale bars*: 1 μm (**A**) and 500 nm (**B**).

equatorial sclera have been reported to be stiffer in glaucoma eyes compared to non-glaucoma eyes by in vivo indirect measurements.[67–69] Experimental IOP elevation in monkeys produces a variably stiffer mechanical response in the overall sclera compared to controls.[70–72] Further estimates of scleral and ONH mechanics have been made by ex vivo inflation testing in animal[73–78] and human[79–83] eyes, which commonly shows far less strain in the sclera than the ONH itself, suggesting lower strain in glaucoma ONH. Strains in postmortem normal human LC decrease with age, and shear strains are larger in the periphery.[43] However, the differences between live and postmortem tissue in thickness and composition suggest the need for testing of living ONH.[84] We and others have developed a method to estimate LC strains in living eyes using OCT and digital volume correlation analysis of radial ONH images after suture lysis

or trabeculectomy.[85,86] This research suggests that glaucoma eyes are not uniformly stiffer in LC strain response to IOP than non-glaucoma eyes. Indeed, mildly damaged glaucoma eyes have lower strains than more severely damaged eyes.[87] This is consistent with our postmortem strain data that showed greater strain in glaucoma eyes with worse damage compared to less damaged eyes.[45] The fact that LC beams were found to be thinner in more advanced OAG eyes in our data supports the conclusion that strains would be greater. Cross-sectional study is limited in drawing conclusions about whether these differences are a pathway followed by glaucoma eyes from normal to mild to severe damage or are characteristics associated with developing only mild damage or leading to severe damage. Longitudinal study of living eyes should be able to identify which is the more correct interpretation.

AO-OCT imaging shows that LC pores of glaucoma eyes take a more tortuous path than in healthy eyes.[88] Indeed, in strains measured by OCT in living glaucoma eyes, shear strains are as large as normal strains, supporting the concept that LC biomechanical movements may derive in part from irregular passage of axon bundles.[89] In 10 normal, postmortem human eyes, SHG images of LC beams were quantified by a method similar to that applied to tissue sections here and compared to measured strains in the same eyes.[44] Strains increased with higher pore area fraction and decreased with denser overlapping beams (nodes). Peripheral regions had lower beam connectivity and higher pore area fraction and tortuosity than the central regions, consistent with their higher strains. In finite element models based on three sheep postmortem eyes, pores near the scleral boundary suffered significantly higher stretch compared to pores in more central regions.[89] In further analysis of postmortem eyes, the curvature of LC was greater in glaucoma eyes, which is also consistent with greater strain (Czerpak, Ling, Jefferys, Quigley, Nguyen, submitted for publication, 2022). Thus, in the normal LC beam network, greater collagen density and connectivity are associated with lower strain, potentially contributing to resistance to glaucomatous damage. In comparing this to our data, we found that peripheral pore area was smaller than centrally. This may be in part due to the use of tissue cross-sections rather than past methods. The configuration of the LC is either that of a curved bowl or of a saddle.[60] Past studies of LC pores by scanning electron microscopy, laser scanning microscopy, or polarized light microscopy or in living eyes by OCT can generate three-dimensional images. Pores in the LC periphery are more likely to be tilted compared to the anterior–posterior axis than those centrally. Thus, pore size might be underestimated with sections perpendicular to this axis, as in the present investigation.

We determined that about half of the volume of the pores carrying axons through the LC consists of astrocyte processes labeled by GFAP. The proportional F-actin volume was nearly the same, suggesting that most actin-labeled processes were those of astrocytes. Furthermore, cells seen within pores by TEM contained intermediate filaments typical for astrocytes. Thus, the contribution of fibroblasts to the changes seen in the pores was difficult to estimate. In a prior investigation in normal monkey ONH by TEM, the proportion of LC axon bundles identified as glia was substantially lower. This could be a species difference, an age difference, or an effect of tissue preparation.[90] In AO-OCT imaging of living eyes, collagen beams were thicker, with greater volume fraction in the central compared to the peripheral
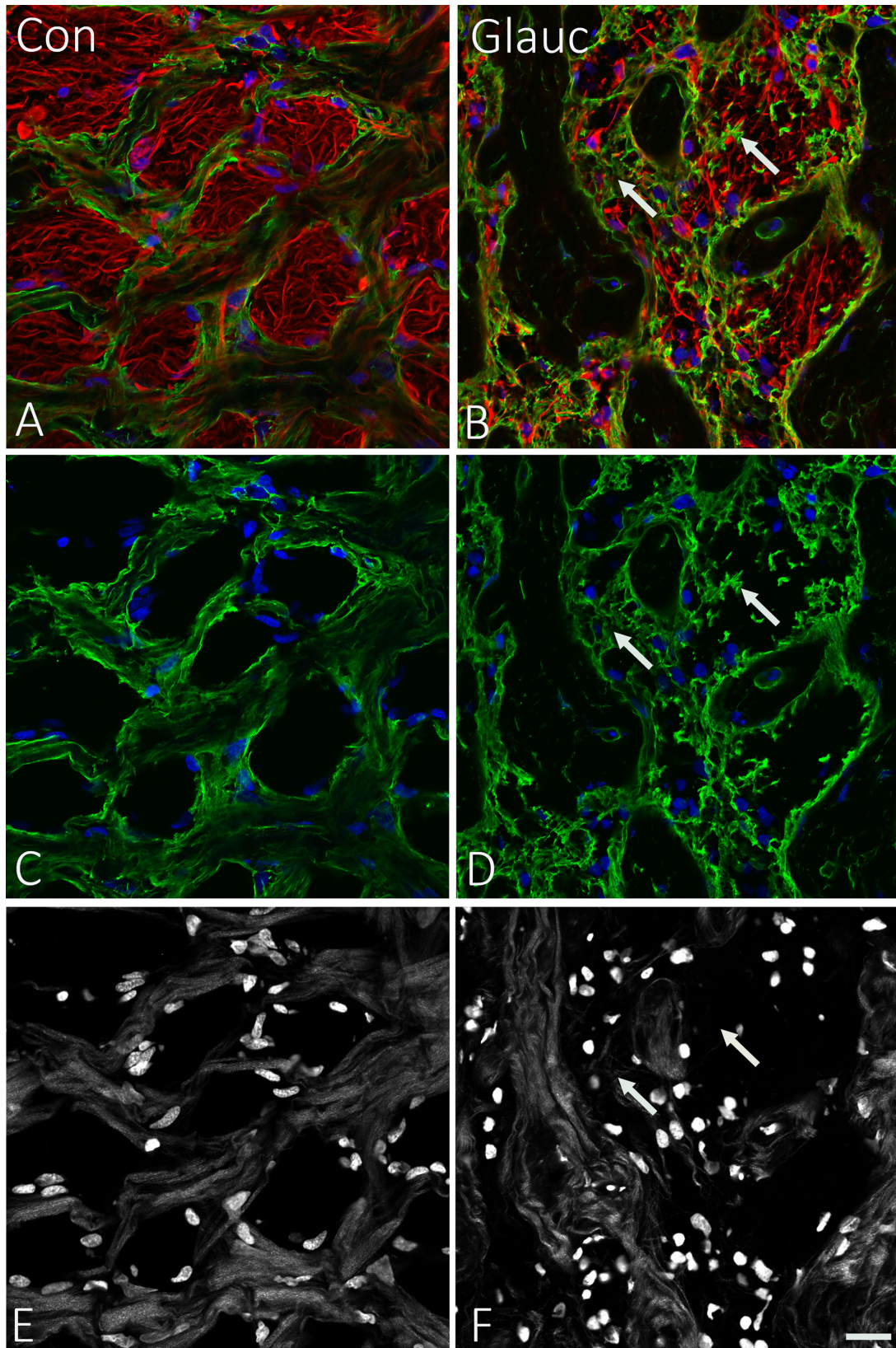
FIGURE 10. Control LC images in *left column* (**A**, **C**, **E**) and glaucoma LC images in *right column* (**B**, **D**, **F**). (**A**) In the control specimen, label for collagen IV (*green*) is seen lining LC beams or within them but not in the pores. GFAP-positive astrocyte processes (*red*) fill the pores. (**B**) In the glaucoma specimen, collagen IV labeling (*arrows*) is prominent within the LC pores (*green*). (**C**) Control eye LC showing collagen IV labeling alone. (**D**) Glaucoma eye LC showing collagen IV abnormally present within the pores (*arrows*). (**E**, **F**) SHG images of same areas showing the position of LC beams. Arrows indicate that collagen IV in **B**, **D**, and **F** is abnormally present within pores. *Scale bar*: 20 µm.

ONH. However, this method can measure only one-third of central and 10% of peripheral LC area.[91] Nonetheless, some of our histological data are quite similar to those from OCT; for example, the mean area of pores was ~1300 μm² in both our material and the OCT images. In two AO-OCT reports on monkey ONH, the mean pore area was two-thirds that of human LC.[25,92] This is consistent with the similarly smaller proportion of the axial length and ONH area of the monkey eye. The strength of tissue sections as in the present study is the ability to label multiple different cellular and extracellular components of the ONH.

This study should be evaluated in the light of several limitations. Although this is one of the largest studies of quantified data on human OAG eyes, the number of eyes and persons is small compared to the prevalence of glaucoma and the diversity of its clinical phenotypes. In particular, the suppliers of eye tissue did not provide data on the derivation and sex of many subjects, preventing us from studying these features as secondary outcomes. Tissues that are collected hours after the person's demise and only fixed or frozen at various times afterward have inevitable autolysis. The TEM evaluations of our specimens, while able to show collagen fibrils and basement membranes that survive postmortem change, did not permit detailed study of astrocyte intracellular structure in most eyes. We did match our non-glaucoma human specimens to the glaucoma eyes by age and time between death and tissue preservation. The cross-sectional nature of the dataset precludes careful causality determination of findings when comparing eyes by degree of optic nerve damage. The regional structure of the human LC beams shows that they are thinner superiorly and inferiorly and oriented radially in the middle and peripheral areas of monkey and human eyes.[4,93] Our present project did not divide the serial cross-section tissue by quadrants, as the ONH orientation had not been preserved. Rather, we divided the cross-section by central versus peripheral regions. Although antibodies to TMEM119 have been reported extensively as specific for microglia, this feature has recently been challenged in the presence of cellular stress.[94]

References

1. Anderson DR, Hendrickson A. Effect of intraocular pressure on rapid axoplasmic transport in monkey optic nerve. *Invest Ophthalmol*. 1974;13:771–783.
2. Vrabec F. Glaucomatous cupping of the human optic disk: a neuro-histologic study. *Albrecht Von Graefes Arch Klin Exp Ophthalmol*. 1976;198(3):223–234.
3. Quigley HA, Addicks EM, Green WR, Maumenee AE. Optic nerve damage in human glaucoma. II. The site of injury and susceptibility to damage. *Arch Ophthalmol*. 1981;99:635–649.
4. Quigley HA, Addicks EM. Regional differences in the structure of the lamina cribrosa and their relation to glaucomatous optic nerve damage. *Arch Ophthalmol*. 1981;99:137–143.
5. Minckler DS, Bunt AH, Johanson GW. Orthograde and retrograde axoplasmic transport during acute ocular hypertension in the monkey. *Invest Ophthalmol Vis Sci*. 1977;16:426–441.
6. Gaasterland D, Tanishima T, Kuwabara T. Axoplasmic flow during chronic experimental glaucoma. I. Light and electron microscopic studies of the monkey optic nervehead during development of glaucomatous cupping. *Invest Ophthalmol Vis Sci*. 1978;17:838–846.
7. Burgoyne CF, Downs JC, Bellezza AJ, Suh J-KF, Hart RT. The optic nerve head as a biomechanical structure: a new paradigm for understanding the role of IOP-related stress and strain in the pathophysiology of glaucomatous optic nerve head damage. *Prog Ret Eye Res*. 2005;24:39–73.
8. Sigal IA, Ethier CR. Biomechanics of the optic nerve head. *Exp Eye Res*. 2009;88:799–807.
9. Quigley HA. The contribution of the sclera and lamina cribrosa to the pathogenesis of glaucoma: diagnostic and treatment implications. *Prog Brain Res*. 2015;220:59–86.
10. Boote C, Sigal IA, Grytz R, Hua Y, Nguyen TD, Girard MJA. Scleral structure and biomechanics. *Prog Retin Eye Res*. 2020;74:100773.
11. Pijanka JK, Coudrillier B, Ziegler K, et al. Quantitative mapping of collagen fiber orientation in nonglaucoma and glaucoma posterior human sclerae. *Invest Ophthalmol Vis Sci*. 2012;53:5258–5270.
12. Yan D, McPheeters S, Johnson G, Utzinger U, Geest JPV. Microstructural differences in the human posterior sclera as a function of age and race. *Invest Ophthalmol Vis Sci*. 2011;52:821–829.
13. Zhang L, Albon J, Jones H, et al. Collagen microstructural factors influencing optic nerve head biomechanics. *Invest Ophthalmol Vis Sci*. 2015;56:2031–2042.
14. Szeto J, Chow A, McCrea L, et al. Regional differences and physiologic behaviors in peripapillary scleral fibroblasts. *Invest Ophthalmol Vis Sci*. 2021;62:27.
15. Emery JM, Landis D, Paton D, Boniuk M, Craig JM. The lamina cribrosa in normal and glaucomatous human eyes. *Trans Am Acad Ophthalmol Otolaryngol*. 1974;78:OP290–OP297.
16. Radius RL, Gonzales M. Anatomy of the lamina cribrosa in human eyes. *Arch Ophthalmol*. 1981;99:2159–2162.
17. Dandona L, Quigley HA, Brown AE, Enger C. Quantitative regional structure of the normal human lamina cribrosa. A racial comparison. *Arch Ophthalmol*. 1990;108:393–398.
18. Jonas JB, Mardin CY, Schlotzer-Schrehardt U, Naumann GOH. Morphometry of the human lamina cribrosa. *Invest Ophthalmol Vis Sci*. 1991;32:401–405.
19. Jan NJ, Lathrop K, Sigal IA. Collagen architecture of the posterior pole: high-resolution wide field of view visualization and analysis using polarized light microscopy. *Invest Ophthalmol Vis Sci*. 2017;58:735–744.
20. Murienne BJ, Chen ML, Quigley HA, Nguyen TD. The contribution of glycosaminoglycans to the mechanical behaviour of the posterior human sclera. *J R Soc Interface*. 2016;13:20160367.
21. Midgett DE, Jefferys JL, Quigley HA, Nguyen TD. The contribution of sulfated glycosaminoglycans to the inflation response of the human optic nerve head. *Invest Ophthalmol Vis Sci*. 2018;59:3144–3154.
22. Quigley HA, Cone FE. Development of diagnostic and treatment strategies for glaucoma through understanding and modification of scleral and lamina cribrosa connective tissue. *Cell Tissue Res*. 2013;353:231–244.

23. Yang H, Williams G, Downs JC, et al. Posterior (outward) migration of the lamina cribrosa and early cupping in monkey experimental glaucoma. *Invest Ophthalmol Vis Sci.* 2011;52:7109–7121.

24. He L, Yang H, Gardiner SK, et al. Longitudinal detection of optic nerve head changes by spectral domain optical coherence tomography in early experimental glaucoma. *Invest Ophthalmol Vis Sci.* 2014;55:574–586.

25. Ivers KM, Sredar N, Patel NB, et al. In vivo changes in lamina cribrosa microarchitecture and optic nerve head structure in early experimental glaucoma. *PLoS One.* 2015;10:e0134223.

26. Strouthidis NG, Fortune B, Yang H, Sigal IA, Burgoyne CF. Longitudinal change detected by spectral domain optical coherence tomography in the optic nerve head and peripapillary retina in experimental glaucoma. *Invest Ophthalmol Vis Sci.* 2011;52:1206–1219.

27. Quigley HA, Dorman-Pease ME, Brown AE. Quantitative study of collagen and elastin of the optic nerve head and sclera in human and experimental monkey glaucoma. *Curr Eye Res.* 1991;10:877–888.

28. Quigley HA, Pease ME, Thibault D. Change in the appearance of elastin in the lamina cribrosa of glaucomatous optic nerve heads. *Graefes Arch Clin Exp Ophthalmol.* 1994;232:257–261.

29. Jones HJ, Girard MJ, White N, et al. Quantitative analysis of three-dimensional fibrillar collagen microstructure within the normal, aged and glaucomatous human optic nerve head. *J R Soc Interface.* 2015;12:20150066.

30. Cone-Kimball E, Nguyen C, Oglesby EN, Pease ME, Steinhart MR, Quigley HA. Scleral structural alterations associated with chronic experimental intraocular pressure elevation in mice. *Mol Vis.* 2013;19:2023–2039.

31. Oglesby EN, Tezel G, Cone-Kimball E, et al. Scleral fibroblast response to experimental glaucoma in mice. *Mol Vis.* 2016;22:82–99.

32. Pitha I, Oglesby E, Chow A, et al. Rho-kinase inhibition reduce myofibroblast differentiation and proliferation of scleral fibroblasts induced by transforming growth factor β and experimental glaucoma. *Transl Vis Sci Technol.* 2018;7:6.

33. Iomdina EN, Tikhomirova NK, Bessmertny AM, et al. Alterations in proteome of human sclera associated with primary open-angle glaucoma involve proteins participating in regulation of the extracellular matrix. *Mol Vis.* 2020;26:623–640.

34. Coudrillier B, Pijanka JK, Jefferys JL, et al. Glaucoma-related changes in the mechanical properties and collagen microarchitecture of the human sclera. *PLoS One.* 2015;10:e0131396.

35. Choi HJ, Sun D, Jakobs TC. Astrocytes in the optic nerve head express putative mechanosensitive channels. *Mol Vis.* 2015;21:749–766.

36. Rogers R, Dharsee M, Ackloo S, Flanagan JG. Proteomics analyses of activated human optic nerve head lamina cribrosa cells following biomechanical strain. *Invest Ophthalmol Vis Sci.* 2012;53:3806–3816.

37. Quillen S, Schaub J, Quigley H, Pease M, Korneva A, Kimball E. Astrocyte responses to experimental glaucoma in mouse optic nerve head. *PLoS One.* 2020;15:e0238104.

38. Xia J, Lim JC, Lu W, et al. Neurons respond directly to mechanical deformation with pannexin-mediated ATP release and autostimulation of P2X7 receptors. *J Physiol.* 2012;590:2285–2304.

39. Kirwan RP, Fenerty CH, Crean J, et al. Influence of cyclical mechanical strain on extracellular matrix gene expression in human lamina cribrosa cells in vitro. *Mol Vis.* 2005;11:798–810.

40. Ogden TE, Duggan J, Danley K, Wilcox M, Minckler DS. Morphometry of nerve fiber bundle pores in the optic nerve head of the human. *Exp Eye Res.* 1988;46:559–578.

41. Winkler M, Jester B, Nien-Shy C, et al. High resolution three dimensional reconstruction of the collagenous matrix of the human optic nerve head. *Br Res Bull.* 2010;81:339–348.

42. Danford FL, Yan D, Dreier RA, Cahir TM, VandeGeest JP. Differences in the region- and depth-dependent microstructural organization in normal versus glaucomatous human posterior sclerae. *Invest Ophthalmol Vis Sci.* 2013;54:7922–7932.

43. Midgett DE, Pease ME, Jefferys JL, et al. The pressure-induced deformation response of the human lamina cribrosa: analysis of regional variations. *Acta Biomater.* 2017;53:123–139.

44. Ling YTT, Shi R, Midgett DE, Jefferys JL, Quigley HA, Nguyen TD. Characterizing the collagen network structure and pressure-induced strains of the human lamina cribrosa. *Invest Ophthalmol Vis Sci.* 2019;60:2406–2422.

45. Midgett D, Liu B, Ling YTT, Jefferys JL, Quigley HA, Nguyen TD. The effects of glaucoma on the pressure-induced strain response of the human lamina cribrosa. *Invest Ophthalmol Vis Sci.* 2020;61:41.

46. Norman RE, Flanagan JG, Sigal IA, Rausch SMK, Terinegg I, Ethier CR. Finite element modeling of the human sclera: influence on optic nerve head biomechanics and connections with glaucoma. *Exp Eye Res.* 2011;93:4–12.

47. Sigal IA, Yang H, Roberts MD, Burgoyne CF, Downs JC. IOP induced lamina cribrosa displacement and scleral canal expansion: an analysis of factor interactions using parameterized eye-specific models. *Invest Ophthalmol Vis Sci.* 2011;52:1896–1907.

48. Kimball EC, Nguyen C, Steinhart MR, et al. Experimental scleral cross-linking increases glaucoma damage in a mouse model. *Exp Eye Res.* 2014;128:129–140.

49. Gerberich BG, Hannon BG, Hejri A, et al. Transpupillary collagen photo-crosslinking for targeted modulation of ocular biomechanics. *Biomaterials.* 2021;271:120735.

50. Quigley HA, Pitha IF, Welsbie DS, et al. Losartan treatment protects retinal ganglion cells and alters scleral remodeling in experimental glaucoma. *PLoS One.* 2015;10:e0141137.

51. Ling YTT, Pease ME, Jefferys JL, Kimball EC, Quigley HA, Nguyen TD. Pressure-induced changes in astrocyte GFAP, actin, and nuclear morphology in mouse optic nerve. *Invest Ophthalmol Vis Sci.* 2020;61:14.

52. Quigley HA, Addicks EM. Chronic experimental glaucoma in primates. II. Effect of extended intraocular pressure elevation on optic nerve head and axonal transport. *Invest Ophthalmol Vis Sci.* 1980;19:137–152.

53. Morrison JC, Dorman-Pease ME, Dunkelberger GR, Quigley HA. Optic nerve head extracellular matrix in primary optic atrophy and experimental glaucoma. *Arch Ophthalmol.* 1990;108:1020–1024.

54. Johnson EC, Morrison JC, Farrell S, Deppmeier L, Moore CG, McGinty MR. The effect of chronically elevated intraocular pressure on the rat optic nerve head extracellular matrix. *Exp Eye Res.* 1996;62:663–674.

55. Hernandez MR. The optic nerve head in glaucoma: role of astrocytes in tissue remodeling. *Prog Retin Eye Res.* 2000;19:297–321.

56. Tehrani S, Johnson EC, Cepurna WO, Morrison JC. Astrocyte processes label for filamentous actin and reorient early within the optic nerve head in a rat glaucoma model. *Invest Ophthalmol Vis Sci.* 2014;55:6945–6952.

57. Korneva A, Kimball EC, Jefferys JL, Quigley HA, Nguyen TD. Biomechanics of the optic nerve head and peripapillary sclera in a mouse model of glaucoma. *J R Soc Interface.* 2020;17:20200708.

58. Korneva A, Kimball EC, Quillen S, et al. Mechanical strain in the mouse astrocytic lamina increases after exposure to recombinant trypsin [published online ahead of print

February 20, 2022]. *Acta Biomater*, https://doi.org/10.1016/j.actbio.2022.02.023.

59. Quigley HA, Hohman RM, Addicks EM, Massof RS, Green WR. Morphologic changes in the lamina cribrosa correlated with neural loss in open-angle glaucoma. *Am J Ophthalmol*. 1983;95:673–691.

60. Thakku SG, Tham YC, Baskaran M, et al. A global shape index to characterize anterior lamina cribrosa morphology and its determinants in healthy Indian eyes. *Invest Ophthalmol Vis Sci*. 2015;56:3604–3614.

61. Morrison JC, L'Hernault NL, Jerdan JA, Quigley HA. Ultrastructural location of extracellular matrix components in the optic nerve head. *Arch Ophthalmol*. 1989;107:123–129.

62. Fukuchi T, Sawaguchi S, Yue BYJT, Iwata K, Hara H, Kaiya T. Sulfated proteoglycans in the lamina cribrosa of normal monkey eyes and monkey eyes with laser-induced glaucoma. *Exp Eye Res*. 1994;58:231–244.

63. Albon J, Karwatowski WSS, Easty DL, Sims TJ, Duance VC. Age related changes in the non-collagenous components of the extracellular matrix of the human lamina cribrosa. *Br J Ophthalmol*. 2000;84:311–317.

64. Quigley HA, Brown A, Dorman-Pease ME. Alterations in elastin of the optic nerve head in human and experimental glaucoma. *Br J Ophthalmol*. 1991;75:552–557.

65. Quigley EN, Quigley HA, Pease ME, Kerrigan LA. Quantitative studies of elastin in the optic nerve heads of persons with open-angle glaucoma. *Ophthalmology*. 1996;103:1680–1685.

66. Wang B, Nevins JE, Nadler Z, et al. In vivo lamina cribrosa microarchitecture in healthy and glaucomatous eyes as assessed by optical coherence tomography. *Invest Ophthalmol Vis Sci*. 2013;54:8270–8274.

67. Hommer A, Fuchsjager-Mayrl G, Resch H, Vass C, Garhofer G, Schmetterer L. Estimation of ocular rigidity based on measurement of pulse amplitude using pneumotonometry and fundus pulse using laser interferometry in glaucoma. *Invest Ophthalmol Vis Sci*. 2008;49:4046–4050.

68. Wang J, Freeman EE, Descovich D, et al. Estimation of ocular rigidity in glaucoma using ocular pulse amplitude and pulsatile choroidal blood flow. *Invest Ophthalmol Vis Sci*. 2013;54:1706–1711.

69. Xiao C, Huang X, Li M, Wu J, Huang H. Evaluation of the biomechanical properties of the posterior eye using shear wave elastography in patients with increased intracranial pressure. *Med Ultrason*. 2021;23:305–310.

70. Downs JC, Suh J-KF, Thomas KA, Bellezza AJ, Hart RT, Burgoyne CF. Viscoelastic material properties of the peripapillary sclera in normal and early-glaucoma monkey eyes. *Invest Ophthalmol Vis Sci*. 2005;46:540–546.

71. Girard MJA, Suh J-KF, Bottlang M, Burgoyne CF, Downs JC. Biomechanical changes in the sclera of monkey eyes exposed to chronic IOP elevations. *Invest Ophthalmol Vis Sci*. 2011;52:5656–5669.

72. Fazio MA, Girard MJA, Lee W, Morris JS, Burgoyne CF, Downs JC. The relationship between scleral strain change and differential cumulative intraocular pressure exposure in the nonhuman primate chronic ocular hypertension model. *Invest Ophthalmol Vis Sci*. 2019;60:4141–4150.

73. Nguyen C, Midgett D, Kimball E, et al. Age-related changes in quantitative strain of mouse astrocytic lamina cribrosa and peripapillary sclera using confocal microscopy in an explant model. *Invest Ophthalmol Vis Sci*. 2018;59:5157–5166.

74. Schwaner SA, Feola AJ, Ethier CR. Factors affecting optic nerve head biomechanics in a rat model of glaucoma. *J R Soc Interface*. 2020;17:20190695.

75. Safa BN, Read AT, Ethier CR. Assessment of the viscoelastic mechanical properties of the porcine optic nerve head using micromechanical testing and finite element modeling. *Acta Biomater*. 2021;134:379–387.

76. Boazak EM, d'Humieres J, Read AT, Ethier CR. Compressive mechanical properties of rat and pig optic nerve head. *J Biomech*. 2019;93:204–208.

77. Du Z, Li R, Qian X, et al. Quantitative confocal optical coherence elastography for evaluating biomechanics of optic nerve head using Lamb wave model. *Neurophotonics*. 2019;6:041112.

78. Ma Y, Pavlatos E, Clayson T, Kwok S, Pan X, Liu J. Three-dimensional inflation response of porcine optic nerve head using high-frequency ultrasound elastography. *J Biomech Eng*. 2020;142:051013.

79. Zeimer RC, Ogura Y. The relation between glaucomatous damage and optic nerve head mechanical compliance. *Arch Ophthalmol*. 1989;107:1232–1234.

80. Coudrillier B, Tian J, Alexander S, Myers KM, Quigley HA, Nguyen TD. Biomechanics of the human posterior sclera: age and glaucoma-related changes measured using inflation testing. *Invest Ophthalmol Vis Sci*. 2012;53:1714–1728.

81. Sigal IA, Grimm JL, Jan N-J, Reid K, Minckler DS, Brown DJ. Eye-specific IOP-induced displacements and deformations of human lamina cribrosa. *Invest Ophthalmol Vis Sci*. 2014;55:1–15.

82. Behkam R, Kollech HG, Jana A., et al. Racioethnic differences in the biomechanical response of the lamina cribrosa. *Acta Biomater*. 2019;88:131–140.

83. Midgett DE, Jefferys JL, Quigley HA, Nguyen TD. The inflation response of the human lamina cribrosa and sclera: analysis of deformation and interaction. *Acta Biomater*. 2020;106:225–241.

84. Fazio MA, Gardiner SK, Bruno L, et al. Histologic validation of optical coherence tomography-based three-dimensional morphometric measurements of the human optic nerve head: methodology and preliminary results. *Exp Eye Res*. 2021;205:108475.

85. Girard MJA, Strouthidis NG, Desjardins A, Mari JM, Ethier CR. In vivo optic nerve head biomechanics: performance testing of a three-dimensional tracking algorithm. *J R Soc Interface*. 2013;10:20130459.

86. Midgett DE, Quigley HA, Nguyen TD. In vivo characterization of the deformation of the human optic nerve head using optical coherence tomography and digital volume correlation. *Acta Biomater*. 2019;96:385–399.

87. Czerpak CA, Kashaf MS, Zimmerman BK, Quigley HA, Nguyen TD. The strain response to intraocular pressure decrease in the lamina cribrosa of glaucoma patients [published online ahead of print July 19, 2022]. *Ophthalmol Glaucoma*, https://doi.org/10.1016/j.ogla.2022.07.005.

88. Wang B, Lucy KA, Schuman JS, et al. Decreased lamina cribrosa beam thickness and pore diameter relative to distance from the central retinal vessel trunk. *Invest Ophthalmol Vis Sci*. 2016;57:3088–3092.

89. Voorhees AP, Jan N-J, Sigal IA. Effects of collagen microstructure and material properties on the deformation of the neural tissues of the lamina cribrosa. *Acta Biomater*. 2017;58:278–290.

90. Minckler DS, Mclean IW, Tso MOM. Distribution of axonal and glial elements in the Rhesus optic nerve head studied by electron microscopy. *Am J Ophthalmol*. 1976;82:179–187.

91. Nadler Z, Wang B, Schuman JS, et al. In vivo three-dimensional characterization of the healthy human lamina cribrosa with adaptive optics spectral-domain optical coherence tomography. *Invest Ophthalmol Vis Sci*. 2014;55:6459–6466.

92. Vilupuru AS, Rangaswamy NV, Frishman LJ, Smith EL, 3rd, Harwerth RS, Roorda A. Adaptive optics scanning laser ophthalmoscopy for in vivo imaging of lamina cribrosa. *J Opt Soc Am A Opt Image Sci Vis*. 2007;24:1417–1425.

93. Roberts MD, Grau V, Grimm J, et al. Remodeling of the connective tissue microarchitecture of the lamina cribrosa in early experimental glaucoma. *Invest Ophthalmol Vis Sci*. 2009;50:681–690.

94. Vankriekelsvenne E, Chrzanowski U, Manzhula K, et al. Transmembrane protein 110 is neither a specific nor a reliable marker for microglia. *Glia*. 2022;70:1170–1190.